SACLANTCEN REPORT
serial no: SR-304

SACLANT UNDERSEA RESEARCH CENTRE REPORT

DISTRIBUTIONS OF MAGNETIC FIELD VARIATIONS, DIFFERENCES AND RESIDUALS

J. Watermann, J. Lam

February 1999

The SACLANT Undersea Research Centre provides the Supreme Allied Commander Atlantic (SACLANT) with scientific and technical assistance under the terms of its NATO charter, which entered into force on 1 February 1963. Without prejudice to this main task – and under the policy direction of SACLANT – the Centre also renders scientific and technical assistance to the individual NATO nations.

SACLANT Undersea Research Centre
Viale San Bartolomeo 400
19138 San Bartolomeo (SP), Italy

tel: +39-0187-5271
fax: +39-0187-524.600

e-mail: library@saclantc.nato.int

NORTH ATLANTIC TREATY ORGANIZATION

Distributions of Magnetic Field Variations, Differences and Residuals

J. Watermann, J. Lam

The content of this document pertains to work performed under Project 061 1 of the SACLANTCEN Programme of Work. The document has been approved for release by The Director, SACLANTCEN.

Jan L. Spoelstra
Director

intentionally blank page

Distributions of Magnetic Field Variations, Differences and Residuals

J. Watermann, J. Lam

Executive Summary:

The search for submarines by means of **M**agnetic **A**nomaly **D**etection (MAD) is effected by a low–flying aircraft with a magnetometer installed onboard, or, for better sensitivity, mounted on an external boom. The magnetic field produced by a submarine appears as a local quasistatic distortion ("anomaly") of the geomagnetic field. The technique requires a remote reference magnetometer at a fixed place in order to compensate for the omni–present temporal variations of the geomagnetic field. This place may be many kilometres away from the position of the aircraft, in which case the technique requires a high spatial uniformity of the ambient magnetic field variations.

While application of the MAD technique may be possible in many areas, there are some areas where this method must fail. These are either areas with poorly mapped magnetostatic anomalies of small spatial scale, or areas with high levels of non–uniform, man–made magnetic noise. The latter typically include coastal zones with industrial and service centers in the vicinity. We find among them the southern Ligurian coastal zone which is magnetically highly disturbed by a busy electrified railway line. Electric train supply currents leak several kilometres out into the sea and produce non–uniform magnetic field distortions (anomalies) of large amplitude.

We propose to employ in such an area the **M**oving **T**arget **D**etection (MTD) technique. Compared to MAD, the roles of sensor and submarine are inverted. Several magnetometers reside in fixed positions on the sea bottom at suitable array nodes and detect localized temporal magnetic field distortions (such as those created by moving submarines) through comparison between simultaneous measurements from different sensors. Depending on the spatial uniformity of the ambient magnetic field, the sensor spacing may be large or must be small.

We found that in an area some 50 km from the coast, a magnetometer located several kilometres away from the zone kept under surveillance, can provide for a good magnetic field reference and is not influenced by the magnetic field of a submarine navigating in the surveillance area. In the southern Ligurian coastal zone, reference magnetometers must be very close to the area under surveillance (one kilometre or less apart) in order to provide for satisfactory magnetic field compensation. In such a case, the reference sensor may also be influenced by the magnetic field of the submarine, and surveillance by means of magnetic field observations is more complicated. It is nevertheless possible, even with limited computing power.

We found that the vertical component of the ambient magnetic field is difficult to compensate for; it contains large signals not linearly correlated between adjacent sites and can not serve as a suitable detector. The smallest uncorrelated contributions to the magnetic field variations were found when observations of the coast-perpendicular magnetic field component from sites at equal distance from the coast were compared. Surveillance arrays should therefore be sited to form pairs with magnetometers at equal distance from the coast.

For the type of magnetometers used in our experiment and for arbitrarily selected magnetic field perturbation thresholds, we give the rate at which the specified threshold is likely to be exceeded, due to signals from natural and man-made sources other than surface vessels or submarines. This rate can be considered the false alarm rate of the magnetic surveillance system. To reduce the false alarm rate, the surveillance system operator must increase the detection threshold or reduce the magnetometer spacing. The report concludes with an example in which we specify a threshold of 0.4 nT and 1 km sensor spacing. We show that several false alarms per hour would be issued if the vertical magnetic field component were considered, but practically no false alarm if the coast-perpendicular component of a pair of magnetometers at equal distance from the coast were considered.

One of the critical issues in designing a magnetic surveillance system is the selection of the magnetometer type. Our observations in the coastal zone suggest that the spatial non-uniformity of the magnetic field requires sensors with small spacing (not more than one kilometre) for satisfactory ambient magnetic field compensation. This implies in many cases a large number of sensors. Sophisticated instruments with extremely low noise and high stability characteristics are less useful. Compensation works best if all three vector components of the magnetic field are used. This requires the use of tri-axial sensors rather than scalar magnetometers.

We need to emphasize that these results are area-specific. Once an area has been selected for magnetic surveillance, magnetic field measurements using at least two spaced sensors must be made prior to deploying the surveillance system, in order to determine which arrangement of magnetometers and which magnetic field component is best suited for surveillance purposes. Such a preparatory survey would typically require a few days of measurements (at least one or two full days), preferably continuously. Due to the physical properties of the ambient magnetic field close to the coast, the vertical component will probably never be very useful. We also expect that the strike direction of the coast will usually favour an arrangement which builds on the correlation between sensors at the same distance from the coast.

This report demonstrates that the efficiency of a magnetic surveillance system using an array of fixed sensors (which we call the MTD technique) depends largely on the arrangement of the sensors relative to the coast and on the magnetic field vector component selected for detecting a passing submarine.

Distributions of Magnetic Field Variations, Differences and Residuals

J. Watermann, J. Lam

Abstract:

Temporal and spatial variations of the geomagnetic field were recorded in different geographic areas, using arrays of seven tri-axial magnetometers on the sea bottom at 50–150 m depth for periods of up to 16 days. The different geographic areas are characterized by different levels of the mean ambient magnetic noise. We discuss data from a magnetically quiet area and then focus on a coastal zone highly disturbed by anthropogenic magnetic fields, in particular by noise from an electrified railway line. In the latter area, the spatial uniformity of the ambient magnetic field is rather poor and the correlation between adjacent sites lower than in the former one.

Simultaneous magnetic field observations from pairs of neighbouring magnetometers are analysed and compared. We compute first vector differences of the magnetic variations measured at neighbouring sites, and subsequently vector residuals. The residuals are those contributions to the magnetic field variations which are not correlated between adjacent sites and which can not be represented through a linear trivariate model.

In the magnetically quiet area, we find that the magnetic field residuals are of the order of the system noise for magnetometers with about 1 km spacing and slightly higher for those with 12 km spacing. The area lends support to the application of a *Remote Reference Technique*, i.e. a technique in which the ambient magnetic field is compensated for by using measurements from a remotely operated reference sensor. "Remote" means that the reference sensor is sufficiently distant not to be influenced by the magnetic field of a ship navigating in the vicinity of the surveillance magnetometers.

Although the magnetic field variations in the highly disturbed coastal zone are several times greater than typical magnetic field variations of natural origin, and also spatially non-uniform, we find good linear correlation between adjacent sites. This is demonstrated by the often rather small magnetic field residuals. However, in order to achieve small residuals, the spacing between the magnetometers must be an order of magnitude smaller than in the quiet zone. This may require the use of a *Local Reference Technique* for compensation of the ambient magnetic field. In a *Local Reference Technique*, the reference sensor must be so close to the surveillance sensors that it, too, is influenced by the magnetic field of the submarine navigating in the vicinity of the surveillance sensors.

In the coastal zone, we find that the residuals of the vertical component of the magnetic field variations remain rather large. The coast–perpendicular component of magnetometers at equal distance from the coast yields the smallest residuals, i.e. they yield the best compensation of magnetic field variations when using a reference technique. The intensity distribution of magnetic field variations observed at the various sites strongly suggests that a significant part of the electric leakage from the railway system flows out into the sea up to several kilometres from shore.

In summary, we find that magnetic field variations in the southern Ligurian coastal zone are dominated by magnetic railway noise which results in an anisotropic distribution of the spatial correlation between spaced sites.

Contents

intentionally blank page

1

Introduction

The steel mass of a ship provides for a magnetic field which is superimposed on the existing ambient magnetic field and modifies it locally. This modification is detectable with commercially available magnetometers at ranges of hundreds of metres and sometimes up to a few kilometres. A ship's magnetic moment consists of two components, a permanent one and an induced one. With respect to their magnetization and, consequently, their magnetic signature, there is no difference in principle between surface vessels and submarines.

The permanent magnetic moment is impressed on the steel in the production process, at the time when its temperature falls below the Curie point. "Permanent" in the sense used here does not imply that it absolutely never changes. However, permanently magnetized material needs to be exposed to a constant magnetic field over a long time (several months, and sometimes even years) in order to acquire, at least partially, a magnetic moment having the orientation of the applied ambient field and thus changing the material's effective moment. The same holds for the decay of the permanent magnetic moment.

The induced magnetic moment varies instantaneously with the intensity and orientation of the ambient field to which the material is exposed. In the open sea, the dominant ambient magnetic field is the geomagnetic field, 99.9% of which stem from quasi–permanent internal sources (their variations are usually called "secular" because they become significant only over a period of many years). This implies that the induced magnetic moment changes with the position of the vessel with respect to its "geomagnetic coordinates".

"Geomagnetic coordinates" is used here as a loosely defined, generic name. Many different geomagnetic coordinate systems with different properties exist. For the purpose of getting a sufficiently accurate quantitative representation of the geomagnetic field at any given geographic position, altitude above sea level, and geomagnetic epoch, the International Geomagnetic Reference Field (IGRF) [1] is a good source to start with. It represents the internal global component of the geomagnetic field and is updated every five years. The presently valid version, the IGRF–95, covers the years 1945 through 2000. The IGRF uses a spherical harmonic expansion up to degree and order 10 and can therefore not very well represent regional and local magnetic anomalies. Regional geomagnetic field models have been compiled for

various parts of the earth, including the Central Mediterranean area (i.e. Italy and surrounding seas), for which an expansion in spatial spherical harmonics of degree four and order two and in temporal polynomials of degree three exists [2]. Regional geomagnetic field models for Germany are published by the ministry of transport [3]. The local magnetic field can usually be taken from anomaly maps where available, with reasonably accuracy and resolution in the vicinity of land masses where the density of measurements is often high, less accurate in the open sea where measurements are sparse. For Italy and the Ligurian, Tyrrhenian, Ionic and Adriatic Seas, magnetic anomaly maps are periodically published, e.g. [4].

If the internal sources were the only ones which determine the intensity and orientation of the geomagnetic field, the problem of detecting a steel-hulled vessel by observing its magnetic signature were reduced to determining as accurately as possible the ambient magnetic field at a given location in absence of ships, and then use this information as the standard against which subsequent magnetic field measurements (at the same location) are to be compared. Any deviation from the standard would then be explained by the presence of a magnetic source subsequently introduced into the area, such as a ship bearing a magnetic moment. In reality, the ambient magnetic field in a marine environment is composed of contributions from various types of magnetic field sources: (a) quasi-permanent sources of internal and anthropogenic origin; (b) oceanic sources, moderately variable in space and time; (c) extraterrestrial sources, highly variable in time, much less variable in space; (d) anthropogenic sources, highly variable in space and time.

Two principally different magnetic detection techniques are nowadays in use. One is known by the acronym MAD (**M**agnetic **A**nomaly **D**etection). In this technique, large areas of the sea are magnetically surveyed by planes. If a submarine is present, its magnetic field is observed as a local deviation of the total magnetic field from its undisturbed level, i.e. the submarine is considered a local magnetic anomaly. If the existing magnetic anomalies such as ship wrecks, pipelines, power cables, or geologically complex sea bed structures, are known, or if the sea is sufficiently deep so that their effect can not be observed at the surface, any previously unknown anomaly can be identified and possibly related to a submarine if no surface vessel is observed. Because the planes fly many times faster than submarines move, this technique means essentially searching with a moving magnetometer for a static magnetic anomaly.

The other technique which is explored at SACLANTCEN, inverts the roles of sensor and target. A magnetometer is installed on the sea bottom, fixed in location and attitude, and records temporal variations of the ambient magnetic field. Those magnetic anomalies which remain fixed in place are not noticed by the magnetometer. Only a moving target, e.g. a moving submarine, which represents a moving magnetic moment, generates a time dependent magnetic field and leaves a signal at the magnetometer. We will use the acronym MTD (**M**oving **T**arget **D**etection) for this technique. Ambient magnetic field sources of type (a) from the list above play

no role in the MTD technique but they may have a significant impact on the MAD technique.

So far, the MAD technique employs in practice sensors which measure only the magnetic field intensity but not its orientation. This restriction is imposed by a sensor attitude control problem. A rotation of a vector magnetometer by just four arcseconds can have the same effect on the measurements as a change of the ambient magnetic field by 1 nT (nanoTesla). For comparison, a typical 1500–ton submarine not treated for magnetic compensation would generate a magnetic field of 1 nT at some 300 m range. A sensor fixed on the sea bottom in a stable position can take advantage of measuring the magnetic field variation in all three vector components. Here, only sensor oscillations forced by the moving sea water can pose a problem if insufficient care is taken [5].

The positioning problem of the MAD technique is less grave than the attitude problem, but it exists. A plane flying over the Tyrrhenian Sea would measure a change of 1 nT by changing its altitude by 50 m, or its position by 500 m in north–south direction. South of Montecristo, in an area characterized by an intense natural magnetic field anomaly, a horizontal displacement by just 30 m is sufficient to change the observed magnetic field by 1 nT. Obviously, this problem does not exist for a magnetometer residing at a fixed place on the sea bottom.

Potential problems common to both techniques are listed in items (b)–(d) above. For the areas investigated in the SACLANTCEN programme on environmental geomagnetic measurements, it could be demonstrated in [5] that the magnetic dynamo field from sea water motion is detectable but of such small intensity that it is negligible in comparison with the other sources and thus plays no role for the MAD and MTD techniques. Only items (c) and (d), extraterrestrial and variable anthropogenic sources, remain to cause problems. They are the subject of our report.

2

Data Coverage

We discuss in this report magnetic field measurements made on the sea bottom along the southern Ligurian coast (Cruise 1996) and near Isola di Montecristo (Cruise 1997). Area maps are given below (Maps 1 and 2). Tables 1 and 2 list the WGS–84 coordinates, bottom depths, and data recording intervals of those magnetometer modules which were operated and recovered successfully. Our report demonstrates that the near–coast array recorded highly disturbed spatially varying signals resulting from the proximity of an active railway line (Cruise 1996). In contrast, measurements made some 50 kilometres from the coast in an electromagnetically very quiet environment display a high degree of spatial uniformity (Cruise 1997).

Table 1 *1996 Measurements (see also Map 1)*

Module	WGS-84 coordinates	Bottom depth	Data interval (UTC)
M03	44°15.76′ N 009°15.47′ E	116 m	10/08, 14:00–10/14, 11:45
M04	44°05.79′ N 009°35.73′ E	130 m	09/28, 20:00–10/14, 11:45
M06	44°08.20′ N 009°30.79′ E	127 m	09/28, 20:00–10/14, 11:45
M12	44°10.09′ N 009°27.15′ E	132 m	09/28, 20:00–10/14, 11:45
M17	44°12.70′ N 009°29.72′ E	58 m	10/04, 10:00–10/14, 11:45
M18	44°11.98′ N 009°29.12′ E	83 m	09/28, 20:00–10/14, 11:45
M19	44°11.11′ N 009°28.26′ E	108 m	09/28, 20:00–10/14, 11:45

We used in both sea trials the same type of autonomous **O**cean **B**ottom **M**agnetometers (OBMs). They are complex modules which integrate a tri–axial linear–core AC–coupled fluxgate magnetometer, two ±25° inclinometers aligned with the x– and y–axes of the magnetic field sensor, and a 2–D fluxgate compass mounted parallel to the x–y–plane which serves to identify the magnetic bearing of the sensor's x–axis once the module has settled on the sea bottom. A crystal oscillator with ±1 ppm long–term stability controls the digital data acquisition system. The manufacturer's design of the fluxgate feedback circuit and our setting of the operating parameters result in a sampling rate of 2 Hz and a usable frequency bandwidth of 1–500 mHz. The data are recorded in 16–bit resolution, with the least significant bit equaling 3.05 pT (picoTesla), and stored in non–volatile solid state memory (flash memory

Table 2 *1997 Measurements (see also Map 2)*

Module	WGS-84 coordinates	Bottom depth	Data interval (UTC)
M03	42°21.88′ N 010°18.70′ E	159 m	07/18, 09:30–08/02, 01:00
M04	42°21.82′ N 010°18.70′ E	159 m	07/18, 09:00–07/26, 11:45
M06	42°21.66′ N 010°18.70′ E	157 m	acuisition failed
M12	42°21.55′ N 010°18.71′ E	144 m	very noisy 30% of the time
M17	42°23.95′ N 010°10.50′ E	134 m	07/19, 14:30–07/26, 13:15
M18	42°24.15′ N 010°10.50′ E	134 m	07/19, 15:00–07/26, 13:30
M19	42°24.55′ N 010°10.50′ E	132 m	07/19, 15:30–07/26, 13:45

cards). Upon retrieval of the modules, the data are transferred from the flash cards to an IBM compatible PC and subsequently written to CD–ROM.

3

The Submarine Magnetic Field

The magnetization of a submarine can be represented by a series of magnetic multipoles with common origin. According to widely accepted theory ($\nabla \cdot \mathbf{B} = 0$), no magnetic monopoles exist, therefore the dipole is the lowest order contribution to the multipole expansion series. The next higher multipole, the quadrupole, can be eliminated from the spherical harmonics expansion if the z–axis of the reference coordinate system is aligned with the dipole moment and the location of the magnetic origin properly selected [6]. The submarine's center of gravity, for instance, would not normally be a good choice for its magnetic origin. The submarine's magnetic field, $\mathbf{B}^{(sm)}$, can thus be written in the form

$$\mathbf{B}^{(sm)} = \frac{\mu_0}{4\pi}\left[\frac{3(\mathbf{M}\cdot\hat{\mathbf{r}})\hat{\mathbf{r}} - \mathbf{M}}{r^3} + O\left(\frac{1}{r^5}\right)\right] \tag{1}$$

$\mathbf{M}$ denotes the dipole moment, $\mathbf{r}$ the distance vector from the submarine's magnetic center to the magnetometer ($\hat{\mathbf{r}}$ the corresponding unit length vector), and *O(f)* means that the rest of the series is asymptotically limited by the function f times a constant factor. Obviously, the effect of the octopole and higher multipoles decreases rapidly with increasing distance between submarine and magnetometer. A rule of thumb which was derived from measurements on cars and ships suggests that for a distance in excess of about 1.5 times the length of the object, only the dipole moment remains to be of significance. An accurate quantitative statement, however, depends on the magnetization of the individual object and would need to be confirmed by specific measurements. Such measurements have not been made at SACLANTCEN. Magnetic signatures from USN submarines, collected by NRaD and analyzed by Hughes Aircraft [7], indicate that the higher multipoles may have some bearing on the composition of those signals which were observed at close distance (some 100 feet), but quantitative results were not given. It is also not the purpose of this report to comment quantitatively on the relative importance of the magnetic octopole and higher multipoles.

Let us assume that the magnetometer is always sufficiently far from the submarine so that it observes only its dipole field while the field from the higher multipoles is absorbed in the system noise. We can then represent each of the three vector components of the magnetic perturbation generated by a submarine sailing along

a straight line with constant speed, through a linear combination of three simple functions named "Anderson functions":

$$\begin{aligned} A_0(\tau) &= (\tau^2+1)^{-5/2} \\ A_1(\tau) &= \tau(\tau^2+1)^{-5/2} \\ A_2(\tau) &= \tau^2(\tau^2+1)^{-5/2} \end{aligned} \tag{2}$$

The dimensionless parameter

$$\tau = \frac{v_0}{r_0}t \tag{3}$$

relates submarine speed, v_0, and distance of closest approach, r_0, to the elapsed time, t, centered on the time of closest approach [8].

Fig. 1 is a graphical representation of the Anderson functions, using the parameters, submarine speed, 6 knts, and distance at closest approach, 300 m. Theoretically, the magnetic field variation seen by each of the three axes of a vector magnetometer consists of a linear combination of these three functions, with coefficients depending on the orientation of the dipole moment relative to the major axis of the submarine and the submarine's course. When looking for the magnetic signature of a submarine one needs to look for magnetic field transients composed of the Anderson functions.

We have no reason to assume that the dipole moment of a ship is oriented parallel to its major axis (i.e. along a horizontal line from bow to stern). It can, in fact, have any arbitrary direction, depending on the history of the vessel (which affects its permanent magnetization) and its actual location and orientation (which determines its induced magnetization.

An example, based on measurements made in 1997, close to Isola di Montecristo, is shown in Fig. 2 (see Map 2 for reference). The SACLANTCEN workboat MANNING sailed with a constant speed of 10.3 knts on a straight west–east course right over OBM 04, which resided 1.5 km north of the island at 159 m depth. The boat crossed it at 14:38 UTC. A second sensor, OBM 03, was located 110 m north of OBM 04, also at 159 m depth. Only the vector residuals between OBMs 03 and 04, and between those two and a third sensor, OBM 19, located 12 km northwest of the former two, are displayed while the uncompensated magnetic field variations, which are an order of magnitude larger, are suppressed here. The residuals are basically differences between magnetic field vectors from two sensors, computed after optimal alignment and linear scaling of the vector components. Thus, the residual is what remains after optimal linear magnetic field compensation with the help of a reference sensor. The term "optimal alignment and linear scaling" is explained more precisely in a subsequent section. The residuals to OBM 19 (blue and green lines) suggest that MANNING's magnetic dipole moment was confined to an east–vertical plane and

pointed almost vertically downward, i.e. it was not aligned with the geomagnetic field. We conclude that MANNING's magnetic dipole moment is dominated by its permanent component while the induced one is negligible.

A rule of thumb, derived from measurements on various vessels and submarines reported in the classified literature, suggests that the magnetic moment of an untreated ship corresponds to about 400 $A{\cdot}m^2$ times the steel mass (in tons) of the ship. According to this rule, the magnetic dipole field of MANNING, as it is seen by OBM 04, should amount to about 1.6 nT, 50% more than the 1.1 nT actually observed. At the location of OBM 03 we would have expected about 0.9 nT as opposed to the 0.7 nT actually observed.

The same rule of thumb provides for an estimate of the detection range for a submarine by means of magnetic field sensors. If the effective ambient noise plus the instrument noise remain below 0.25 nT in the frequency band of interest, and the detection threshold is set to 0.25 nT, a 1500–ton submarine might be detected if it passes the sensor within a range of some 600 m. The rule of thumb can also be used to estimate the time interval a submarine navigates within the detection range. If our sample submarine sails with 100 m clearance at 6 knts speed directly over the magnetometer, its magnetic field would exceed 0.25 nT for a period of about 6 minutes.

4

Magnetic Field Reference Techniques

A permanently present background of natural magnetic field fluctuations covering a wide frequency band, including the frequency band of interest to ASW, provides for a level of magnetic ambient noise the intensity of which is usually much higher than the sensitivity of the magnetometers. Fig. 3, compiled from data found in [9], [10], shows a distribution of the mean peak–to–peak amplitudes of geomagnetic *pc1–pc5* fluctuations, observed over many years in Central Europe (more specifically, in the vicinity of Göttingen, F.R.G.). "Mean amplitude" means that an average was taken over all those time intervals in which fluctuations within a given, narrow frequency band could be identified. Consequently, geomagnetic ULF fluctuations possess at times amplitudes exceeding the mean values displayed here. The *pc* type of ULF fluctuations is just one specific type (and usually not the most intense one) of a wide range of different types of geomagnetic field fluctuations, and is observed practically every day, and often for many hours.

Fig. 1 demonstrates that, for the submarine parameters assumed here, the magnetic field perturbation would have a typical duration of 300–400 seconds. From Fig. 3 we learn that geomagnetic *pc* fluctuations in the corresponding period range reach an average amplitude of 6 nT p–p. Such an amplitude would be equivalent to a magnetic signal from our sample submarine navigating at less than 200 m range. In order to increase the detection range, a technique has to be developed which aids in suppressing the effect of the geomagnetic fluctuations.

Building on the fact that the most important contribution to the natural geomagnetic fluctuations stems from sources in the ionosphere and magnetosphere, more than 100 km above the ground, and the second important contribution from non–uniform conductivity distributions found at geographic discontinuities such as coast lines, we can assume that in most areas the spatial uniformity of the natural geomagnetic fluctuations is sufficiently high over a distance of at least a few kilometres to permit simple linear magnetic field compensation. A more detailed discussion follows further below, along with the presentation of magnetic field data from the 1997 cruise.

The spatial uniformity of the geomagnetic field fluctuations is employed in compiling the example shown in Fig. 4. Fig. 4a displays vector time series from two different events recorded by OBM 04 in September 1995 in the vicinity of the Formiche di

Grosseto group of islands (see Map 3 for reference). In each panel, a section is highlighted which could, according to Fig. 1, possibly be associated with a passing vessel. Fig. 4b displays a stack of simultaneous measurements from three magnetometers (eastward components only), spanning a distance of eight kilometres (c.f. Map 3). The upper panel of Fig. 4b reveals that the suspicious signal observed on September 16 around 18:41 UTC appeared at all three sites with almost identical amplitude and shape. The mean difference field (the difference between OBM 04 and a weighted mean of OBMs 18 and 19) is not particularly enhanced. A ship signature can therefore be excluded. At 8 km distance, even a ship with 100,000 tons of steel mass would generate a magnetic field of a couple of pT (picoTesla) only, much less than the system noise of our magnetometers. The lower panel, however, demonstrates that the suspicious signal observed on September 20 at 08:46/:47 UTC was seen only by OBM 04 and not by the OBMs 18 and 19. It must have been generated by a local source, for which we suggest a passing vessel.

Fig. 4 demonstrates that fluctuations of the ambient magnetic field can be compensated for by using a reference magnetometer as long as its distance from the surveillance magnetometer (termed "test magnetometer" in the following) is significantly smaller than the spatial scale length of the ambient magnetic field fluctuations. This may in some cases permit to choose a distance which exceeds the range within which the ship generates a measurable signal. In such a case, when the test magnetometer records a magnetic signal from a ship, the reference magnetometer is free of such a signal and thus provides for a proper magnetic field baseline. We term this the *Remote Reference Technique*. Fig. 2 may serve as an example for this technique (blue and green lines). OBMs 03 and 04 record the magnetic signature of the workboat MANNING while OBM 19, 12 km away, is guaranteed free from any magnetic influence by MANNING. The residual shows MANNING's true magnetic signature. It appears of larger amplitude at OBM 04, and of smaller but still detectable amplitude at OBM 03.

In other cases, when the ambient magnetic field is less uniform, a satisfactory ambient magnetic field compensation may require a reference magnetometer so close to the test magnetometer that it may be influenced, too, by the ship's magnetic field. We term the technique applied in this case the *Local Reference Technique*. Fig. 2 (red lines) demonstrates its application. OBMs 03 and 04 are both influenced by the magnetic field of MANNING, the residual between the two OBMs is therefore not identical to the true magnetic field perturbation, specifically, it is of smaller amplitude. The residual does thus not provide for a true replica of MANNING's magnetic signature. It is one of the objectives of this report to show that the choice of the proper reference technique depends on the area which is supposed to be kept under surveillance.

5

Data Analysis Method

In performing the data analysis we proceeded with the following steps. After having checked the magnetic field and housekeeping data from the OBMs for consistency, the recorded time stamps were validated. The clocks of the OBMs had been synchronized with a GPS receiver before deployment. At the end of the sea trial, after recovery of the OBMs, their internal clocks were compared against a GPS reference clock. The differences between nominal and actual times are listed in Table 3.

Table 3 *OBM oscillator deviations from GPS standard*

Year	OBM	Operation	Clock offset	Normalized
1996	M03	8 d	−755 ms	−94 ms/d
	M04	20 d	+125 ms	+6 ms/d
	M06	20 d	−220 ms	−11 ms/d
	M12	20 d	+1230 ms	+62 ms/d
	M17	16 d	−75 ms	−5 ms/d
	M18	20 d	−175 ms	−9 ms/d
	M19	20 d	+65 ms	+3 ms/d
1997	M04	16 d	−100 ms	−6 ms/d
	M12	16 d	+590 ms	+37 ms/d
	M17	16 d	−530 ms	−33 ms/d
	M18	16 d	−500 ms	−31 ms/d
	M19	16 d	−575 ms	−36 ms/d

All housekeeping data were exhaustively scrutinized, not just spotchecked. It was verified that the time stamps were always correctly updated, the temperature remained stable and at a meaningful value, the supply voltages were in the correct range and decreased with time progressing (though very little), the compass bearing and the inclination angles remained stable once the modules had settled on the sea bottom (usually within a few hours after deployment), and the magnetometer x– and y–axes deviated from the horizontal plane by not more than a few degrees. Locations had been selected for deployment where the sea bed was practically horizontal, and this was verified by MANNING's echo sounder.

Once the raw data had been transferred to an IBM type PC, the three components of the magnetic field vector were transformed into a suitable coordinate system. The mathematical formulation of the rotation procedure is given in Annex A. The 1997 measurements were conducted far away from the mainland where no implied preference direction of the magnetic field variations exists. We adapted a coordinate system aligned with the geomagnetic north, east and vertical axes. For the near coast measurements of 1996, we found that the amplitude of the magnetic field variations was related to the orientation of the coast line, with mean amplitudes different between the components parallel and perpendicular to the coast. Therefore it appeared appropriate to use a coordinate system in which the x–axis runs parallel to the mean coast line, the y–axis perpendicular to it, and the z–axis points vertically down.

The magnetic field data were low–pass filtered using a 0.08 Hz (12.5 s) cutoff frequency, decimated to 6 seconds sampling rate, and subsequently high–pass filtered with a cutoff frequency of 0.0015 Hz (667 s). This bandwidth was chosen such that it would normally encompass the magnetic signature of a passing submarine (c.f. Fig. 1). Considering that the clock deviations from their nominal values (Table 3) were always at least an order of magnitude smaller than the low–pass cutoff period, no need arose for a correction of the OBM time stamps.

The magnetic field variations observed close to the coast are largely determined by train noise from a busy coastal railway line (180 trains per day) which tends to follow a pronounced diurnal pattern. Diurnal magnetic field intensity distributions were derived from 16 days of continuous land–based measurements near Deiva Marina, made by a former SACLANTCEN summer student, A. Magunia, in September/October 1996, during our sea trial. The result is displayed in Fig. 5 in a self–normalized gray scale (A. Magunia, J.W.Goethe–Universitt, Frankfurt/Main, private communication). Based on this distribution of the magnetic field disturbance level, more specifically, the magnetic field variance over subsequent 15–min sections, each day was devided into four intervals which are listed in Table 4.

Table 4 *Diurnal intervals according to train traffic*

Time interval (UTC)	Characteristics
04:30 – 09:30	moderate train traffic, medium noise
09:30 – 18:00	heavy train traffic, high noise
18:00 – 21:30	moderate train traffic, medium noise
21:30 – 04:30	little train traffic, low noise

For each OBM, each day of operation, and each of the intervals listed in Table 4, the recorded magnetic field variation was centred to yield zero mean. Subsequently,

the amplitude difference between two neighbouring OBMs was computed. This method is a simple application of a reference technique. It was improved upon in a subsequent step.

Several error sources, partly device–dependent, partly imposed by nature, render the simple vector difference an unsatisfactory method. Firstly, the OBM compass has only 2° accuracy, i.e. 2° uncertainty, and the inclination measurements have 0.2° resolution and uncertainty. Secondly, the three axes of the fluxgate sensors may not be exactly orthogonal and aligned with the compass and inclinometer axes. Thirdly, the geography (i.e. the distribution of water and land masses) and the geology produce discontinuities of the electrical conductivity distribution and impose certain preferred directions on those electric currents which are induced by the external magnetic field variations. They can contribute significantly to the total magnetic field. Fourthly, the geometry of stray currents resulting from leakage of the train return current is largely dependent on the location of the railway power substations, the orientation of the railway line, and the conductivity structure of the seabed, and may thus have different preference directions at different OBM locations.

In order to alleviate the effect of these errors, a time–domain trivariate linear regression algorithm was applied to the vector time series from pairs of neighbouring OBMs for each of the four diurnal intervals and each day of magnetometer operation. Such a method had also been applied to land–based magnetic field measurements in order to determine the impact of various error sources on the apparent spatial correlation between two adjacent sites [11]. The regression scheme relates the magnetic field variation, $\mathbf{B}^{\mathrm{T}}$, observed by a tri–axial sensor at a test site, to the magnetic field variation, $\mathbf{B}^{\mathrm{R}}$, observed at the same time by a tri–axial sensor at a reference site

$$\begin{pmatrix} {B_x}^T(t) \\ {B_y}^T(t) \\ {B_z}^T(t) \end{pmatrix} = \begin{pmatrix} A_{xx} & A_{xy} & A_{xz} \\ A_{yx} & A_{yy} & A_{yz} \\ A_{zx} & A_{zy} & A_{zz} \end{pmatrix} \cdot \begin{pmatrix} {B_x}^R(t) \\ {B_y}^R(t) \\ {B_z}^R(t) \end{pmatrix} + \begin{pmatrix} \delta{B_x}^T(t) \\ \delta{B_y}^T(t) \\ \delta{B_z}^T(t) \end{pmatrix} \quad (4)$$

The residual vector, $\delta\mathbf{B}^{\mathrm{T}}$, is just of that part of the magnetic field that can not be explained through linear regression between test and reference sensor. If no instrument error or magnetic field non–uniformity would affect the measurements and if the three magnetic field vector components were fully independent from each other, (A_{ij}) were the identity matrix. Increasing deviation of (A_{ij}) from a diagonal matrix is equivalent to an increasing cross–correlation between different vector components. The coefficients of the regression matrix, (A_{ij}), are found by minimizing the sum of the squared error residuals (the elements of the right-most vector on the right hand side of eq. (4)). This procedure results in magnetic field vectors which we call "optimally aligned and scaled". The mathematical procedure for computing the coefficients is described in Annex B.

If the magnetic field variations observed simultaneously by two magnetometers consist of a superposition of signals highly correlated between the two sites, and random noise of equal variance, uncorrelated between the two sites, the error terms are smaller if the magnetometer with the more intense signal is taken as the reference sensor. This is shown in Annex C. In the vicinity of the coast, the train noise is the dominating magnetic signal, the intensity of which decreases with increasing distance from coast. Fig. 6 shows a stack of sample time series from a 3–hour interval, recorded in the fall of 1996 by the OBMs 17, 18, 19 and 12 (c.f. Map 1). Only the coast–perpendicular component is displayed. We notice that the magnetic field variations arer very similar in shape, and the amplitudes decrease with increasing distance from the coast. Consequently, we chose for each pair of magnetometers the one closer to coast as the reference sensor. The 1997 measurements were made far away from the coast, with a group of magnetometers close to Montecristo island and another group off–shore several times the extent of the island. We use OBM 19, one of the latter group, as a reference. The pairs of OBMs selected for analysis are listed in Table 5 (see also Maps 1 and 2). The meaning of Lobs (last column of Table 5) is explained in Annex D.

Table 5 *Pairs of OBMs selected for regression analysis*

Year	Test→Reference	Distance	Connection line	L_{obs}
1996	M18→M17	1.55 km	perpendicular to coast	0.4825 nT
	M19→M18	1.97 km	perpendicular to coast	0.5455 nT
	M12→M19	2.40 km	perpendicular to coast	0.6100 nT
	M06→M12	5.97 km	parallel to coast	1.1455 nT
	M04→M06	7.94 km	parallel to coast	1.4410 nT
	M03→M12	18.73 km	parallel to coast	
1997	M17→M19	1.11 km	south to north	
	M04→M19	12.30 km	south–east to north–west	

For each pairs of neighbouring magnetometers, each day of operation, and each diurnal interval, the sums of the squared absolute and relative error residuals were examined. Time segments having abnormally large residuals were not used in the following step, namely averaging of the matrix coefficients. The number of intervals discarded was very small, they are listed in Table 6. The matrix coefficients of the remaining, "clean" segments, were averaged over consecutive days so that one single transfer matrix resulted for each of the four diurnal intervals and each pair of OBMs. These averaged matrices were used in constructing univariate transfer function models in the time domain, of the type described by eq. (4).

Table 6 *Time segments excluded from regression matrix averaging*

Year	Test→Reference	Time interval (UTC)
1996	M18→M17	Oct 08, 09:30–18:00
	M19→M18	Oct 06, 09:30–18:00
	M12→M19	Oct 06, 09:30–18:00
	M12→M19	Oct 10, 09:30–18:00
	M06→M12	Oct 02, 21:30–Oct 03, 04:30
	M04→M06	Oct 04, 18:00–21:30
	M04→M06	Oct 09, 18:00–21:30
	M03→M12	Oct 10, 18:00–21:30
1997	M17→M19	July 23, 04:30–09:30
	M17→M19	July 23, 09:30–18:00

This method was chosen in order to simulate the data processing in a "real" submarine detection experiment. In such an experiment, a reliable transfer matrix would be determined from "clean" time segments, i.e. time segments not contaminated by passing ships or certain types of sensor noise. The transfer matrix would subsequently be applied in real time to magnetic field measurements coming in from two magnetometers, in order to identify local magnetic field perturbations which appear at only one of the two OBM sites, or at both sites but with different amplitudes and orientations.

In the following discussion we consider one of the two OBMs of each pair the "test magnetometer", measurements from which are confronted to those from a "reference magnetometer". The time series of magnetic field variations measured by the test magnetometer, their difference to the variations measured simultaneously by the reference magnetometer, and the residual time series which remain after trivariate representation through averaged transfer matrices, were binned according to the scheme described below. Different bin sizes, 0.2 nT for the 1996 data and 0.05 nT for the 1997 data, were chosen in order to account for the largely different mean intensity levels of the magnetic variations recorded in the two different areas.

The binning was done individually for each pair of OBMs, each vector component, each day and each diurnal interval individually. It was based on the deviation of the data points from the zero line, irrespective of their sign, whether positive or negative. This means, in effect, counting the number of times the absolute value increased past one of a series of regularly spaced thresholds, and tally the results. Crossings of the zero level were not counted. Fig. 7 illustrates the binning procedure for a fictitious data set and four bin thresholds on each side of the zero line.

A complete set of plots from all pairs of magnetometers listed in Table 5 appears in Fig. 8a–h. Magnetic field variation, difference to the neighbour OBM, and the residual computed for each vector component, are plotted in separate panels. The days are incremented along the abscissa, with each day broken into four columns which represent the four diurnal intervals, and the bins along the ordinate. The decadic logarithm of the number of counts at each bin threshold, normalized to a common time unit of one hour, is displayed using the color code found at the bottom of each page.

Table 7 *Identified disturbances removed from the 1996 data*

Module	Date	Time (UTC)	Description
M03	Oct 10	20:30–20:50	vessel
M04	Sep 30	08:55–09:10	MANNING
	Oct 03	19:20–19:30	vessel
	Oct 04	13:30–13:40	MANNING
	Oct 07	08:25–08:30	vessel
	Oct 08	15:10–15:15	MANNING
	Oct 09	19:40–19:55	vessel
M06	Sep 30	09:30–09:40	MANNING
	Oct 03	00:45–01:05	vessel
	Oct 04	13:00–13:10	MANNING
	Oct 04	19:05–19:15	vessel
	Oct 08	14:35–14:45	MANNING
	Oct 11	14:55–15:05	vessel
M12	Sep 30	10:10–10:20	MANNING
	Oct 04	12:35–12:40	MANNING
	Oct 08	14:10–14:20	MANNING
	Oct 10	10:15–10:25	vessel
M17	Oct 04	12:05–12:15	MANNING
	Oct 08	13:40–13:50	MANNING
M18	Sep 30	15:45–15:55	MANNING
	Oct 04	12:15–12:20	MANNING
	Oct 08	13:50–14:00	MANNING
M19	Sep 30	15:35–15:45	MANNING
	Oct 04	12:20–12:30	MANNING
	Oct 06	14:30–14:40	vessel
	Oct 08	14:00–14:10	MANNING
	Oct 13	20:40–10:45	vessel

The residual panel is split into two sections, the upper one showing the results from all data, the lower one the results after the data had been cleaned for those artificial magnetic field perturbations which could be identified with certainty. Removed in this process were signatures of passing vessels (including site visits by MANNING), acoustic interrogation, individual instrument spikes lasting for one single data point only, and obvious sensor noise of large amplitude, such as abrupt offset changes. Tables 7 and 8 list the data which were removed from the residual time series in order to produce the cleaned residuals.

Table 8 *Identified disturbances removed from the 1997 data*

Module	Date	Time (UTC)	Description
M03	July 23	04:30–04:36	sensor noise
		07:24–07:42	sensor noise
		15:56–15:57	single spike
		18:55–19:05	sensor noise
M04	July 21	14:36–14:40	MANNING
M17	July 20	18:09–18:19	vessel
	July 24	09:40–09:50	vessel
M18	July 24	09:40–09:50	vessel
	July 25	04:35–04:45	sensor noise
M19	July 21	16:41–16:43	single spike
		17:07–17:08	single spike
		17:28–17:29	single spike
	July 23	12:54–12:55	single spike
		17:14–17:16	single spike

6

Distributions of Magnetic Field Variations, Differences and Residuals

The data from the 1997 cruise, taken in an area far away from anthropogenic magnetic field sources, may serve as a manifestation of the "ground state" of magnetic field fluctuations, against which the data taken at magnetically highly disturbed sites along the Ligurian coast (1996 cruise) have to be confronted. We first discuss two data sets from the 1997 cruise (Fig. 8a,b) and then a series of data sets from the 1996 cruise (Fig. 8c–h).

Fig. 8a shows the magnetic field variations observed by OBM 17, and a comparison with the reference magnetometer OBM 19. In the X– and Y–components (northward and eastward) we notice a slight dependence of the magnetic field intensity on the time of the day. It appears to be highest in the first two diurnal intervals (04:30–18:00 UTC, equivalent to 06:30–20:00 local time) and lowest in the forth (21:30–04:30 UTC, 23:30–06:30 local time). Anthropogenic electromagnetic noise originating from Montecristo island, more than 12 km away and with no electromagnetic source but a small Diesel generator, can not be responsible for the diurnal pattern. We conclude that even areas of the Tyrrhenian Sea some 50 km away from the mainland are to a small extent contaminated by anthropogenic magnetic noise. We also notice that the vertical magnetic field component is generally much weaker than the horizontal one. This is typical for a horizontally layered electrical conductivity distribution with a good conductor on the top, such as sea water and water–saturated sediments. The magnetic field difference between OBMs 17 and 19 is much smaller than their magnetic field variations which demonstrates that the variations are to a high degree correlated between both sites. The even smaller residual amplitudes confirm this but uncover also several exceptions.

Two segments bearing large residuals, the second diurnal interval of July 20 and the third of July 21, were found to be affected by the signature of a vessel passing OBM 17, and a group of single spikes was detected in the data of OBM 19 (c.f. Table 8). Otherwise, the residuals remain, with one exception which occured during the second interval of July 20, below the dual–instrument maximum noise level (according to our estimates about 0.25 nT over the frequency band considered here). On July 23, the data from OBM 17 appeared highly disturbed, with a sequence of magnetic field perturbations bearing all the characteristics of instrument noise. Altough the magnetometer tended to recover somewhat, it never returned to the

previous, low noise level, a fact which is particularly well seen in the data from the Z–component (vertical). The effect is well visible in the difference and residuals, in fact, from July 23 on, the Z–component difference and residual remain almost as large as the Z variation of OBM 17. It means that, beginning with July 23, the correlation between the data from the two magnetometers became very small. A possible but not confirmed explanation could be the following. The modules were exposed to direct sunlight and heated up while being prepared for deployment from the workboat, and a valve had to be opened to release the air pressure inside the module which started to build up with the rise of the temperature (36° C peak measured immediately before deployment). The warm, humid air above the water had thus access to the interior of the modules. Once deployed and adjusted to the significantly lower temperature prevailing on the sea bottom (16° C measured), the humid air inside may have condensed to drops which affected negatively the electronic circuitry, despite precautions taken against humidity.

Fig. 8b shows further results from the same cruise. Data from OBM 04 (located close to Montecristo island) are compared to those from OBM 19, i.e. over a distance of more than 12 km. We notice that the residuals between both data sets, after removing the signature of MANNING and the sequence of instrument spikes from the second interval of July 21, rarely exceed 0.5 nT. A comparison with the first four undisturbed days of the OBM pair 17/19 (Fig. 8a) shows that the residuals OBM 04 vs. OBM 19 are only twice as large as the residuals OBM 17 vs. OBM 19. Only around July 24, intense magnetic activity of ionospheric origin led to large natural magnetic field variations which left their traces on the residuals, making them larger than they were during magnetically quiet times. We suggest that the area investigated in 1997 is suitable for application of the *Remote Reference Technique*, with a sensor spacing of the order of 2 to 3 kilometres.

We now turn to the data from the 1996 Ligurian coast cruise, Fig. 8c–h. They reveal various characteristics which are common to all of the OBMs.

- A pronounced and regularly repeated diurnal pattern is observed in all three magnetic field components. Amplitudes of magnetic field variations recorded throughout the 1996 cruise are much larger than those from the 1997 cruise.
- The Y–component (oriented coast–perpendicular) generally exhibits the smallest magnetic field variations, and the Z–component (oriented vertical) the largest.
- When inspecting magnetic field vector differences and residuals between two neigbouring OBMs, the Z–component remains to be the largest one.

The following properties apply only to the OBMs 04, 06, 12, 17, 18 and 19. OBM 03, much farther to the northwest, has to be exempted.

- The vector differences between neighbouring magnetometers (middle row panels of Fig. 8c–g) are smaller than the variations (top row panels) and facilitate detecting signatures of local magnetic sources which affect only one of the two OBMs in a pair.
- The residuals seem to improve upon the differences in the sense that they are significantly smaller than the differences, in particular in the X– and Y–components, less so in the Z–component. This facilitates even more detecting local magnetic field perturbations.

OBM 03 differs from the rest of the array in a particular way:

- The magnetic field differences to the magnetometer closest by, OBM 12, exceed the magnetic field variations, and the residuals are of the same order of magnitude as the variations. Magnetic field variations at the sites of the OBMs 03 and 12 appear to be poorly correlated.

The following propositions are made in order to explain, at least partially, the findings described above.

Natural magnetic field fluctuations are solar–wind driven and are unevenly and irregularly distributed over the day. At midlatitude stations, narrow–banded, continuous types of pulsations prevail on the sunlit side of the earth, and irregular, bursty types on the dark side. Our findings from our coastal OBM array suggest, however, a dominating influence of anthropogenic sources with a rather regular diurnal variation. The Italian state railway system, which uses DC–powered electric engines, is the most likely candidate for their generation [12], [13], [14].

The train engines are powered from substations located along the railway line at a spacing of 10 to 30 kilometres. Part of the return current from the trains flows through the rails back to the substations, but, due to intentional grounding of the rails at regular spacing, another part of the return current leaks and finds other paths. Each time a train accelerates or decelerates, the electric power consumption changes drastically, and the return current to the power substation changes with it. The high intensity of magnetic field variations observed several kilometres from the coast (and from the railway line) indicates that leakage currents reaching far out into the sea must be the source of the major part of the magnetic field variations. A simple calculation reveals that the electric current loop formed by the supply current through the overhead contact wire, the train engine, and the rail return current, can not account for measurable magnetic field variations. Using typical numbers, namely a supply current of 1000 A and a vertical distance between contact wire and rail of 5 m, we find that the magnetic signal strength 2 km away (i.e. at the location of the nearest module, OBM 17) should be 0.25 nT, equal to the dual–sensor self noise.

8 km away from the railway (i.e. at the location of OBM 12), the signal would be only 15 pT and thus undetectable. We conclude that the leakage currents must flow much closer to the OBMs than the rails run (i.e. the currents extend far out into the sea) in order to generate the large magnetic field variations observed by the OBM array.

Let us now consider a northwestbound train starting from La Spezia. Before reaching Levanto the train is powered by the substations of La Spezia and Levanto. La Spezia is located on the remote side of the mountain ridge, and the electrically poorly conducting mountains largely prevent leakage currents between La Spezia and Levanto to reach the sea where the OBM array resides. Thus, only leakage currents between Levanto and the train play a role for OBM 04. When running between Sestri Levante and Levanto the train engine is powered by the substations at the latter two cities, and the return leakage currents flow back to these two substations. OBMs 17, 18, 19, 12 and 06 are thus simultaneously exposed to the currents supplied by and flowing back to Levanto and Sestri Levante, but OBM 03 is not. Once the train passes Sestri Levante, the train engine draws power from the substations of Sestri Levante and San Margherita Ligure, and now OBM 03 is exposed to train leakage currents while the rest of the array is no longer affected by it. Though the large magnetic field differences and residuals between OBM 03 and the rest of the array may be explained this way, we still expect a noticable difference between OBMs 04 and 06. This is not the case, the pairs OBM 04/06 and OBM 06/12 have rather similar difference and residual levels, both of which are much smaller than the variations.

Fig. 9 gives an example of the magnetic disturbance caused by the passage of a single train. During the time interval shown here, only one single train ran between Levanto and Sestri Levante, according to the records of the regional railway administration in Genoa (we did not rely on the official timetable which may be inaccurate). The highlighted sections show when the train was on the rails between Levanto and Sestri Levante (yellow) and when it traversed the railway station of Deiva Marina (green). The train did not stop there, but the large magnetic field offsets indicate that the train did significantly decelerate before and accelerate after the passage.

The coastal effect, which explains the prevention of large–scale electric currents, such as currents induced by natural magnetic fields, from penetrating from the well conducting sea into the poorly conducting coastal mountain range, would result in large vertical magnetic field variations close to the coast [15]. When comparing the upper right panels of Fig. 8c–g one notices some attenuation of the Z variations with increasing distance from the coast (Fig. 8c–e) and practically equal amplitudes at sites having about the same distance from coast (Fig. 8e–g). This observation is consistent with the coastal effect.

The horizontal magnetic field variations show large amplitudes in the X–component (coast–parallel), which decrease with increasing distance from coast and remain approximately constant at constant distance from coast (c.f Fig. 8c–g, upper left panels), and less intense variations in the Y–component (coast–perpendicular). Electric leakage currents from the railway line, if flowing close to the rails, would produce a magnetic field mainly perpendicular to the coast (i.e. in the Y– rather than the X–component). Our observations thus imply that the railway leakage currents reach far out into the sea and confirm the statement we made above.

7

Cumulative Binning of the Distributions

The binned data which had been used to create Fig. 8a–h, were then processed in a different way. Instead of creating distributions for each day and diurnal interval individually, all data from a given pair of magnetometers and a given diurnal interval were accumulated and then normalized to yield threshold crossings per hour ("events/hour"). Only the OBM pair 17/19 (1997 sea trial) was divided into two sections, one prior to July 23, and the other starting from July 23. This was deemed necessary because of the significantly different behaviour of OBM 17 from July 23 on (see discussion above). The OBM pair 03 12 (1996 sea trial) is not included in Fig. 11 because Fig. 8h demonstrates that the residuals were as large as the variations themselves, i.e. there is very little correlation between the two sites. No further comparison is deemed useful.

To facilitate inter–comparison of different OBM pairs from 1996, we normalized the binning results to a distance of 1 km, assuming a linearly increasing difference and residual magnetic field and constant sensor noise. In other words, we display averages of the spatial gradients of the magnetic field differences and residuals, supplemented by system noise. In essence, the distributions were modified according to Annex D, eq. (D3). This procedure incorrectly modifies the magnetic field variations which are per definition single station measures and for which the distance to the neighbouring OBM bears no meaning. In particular, a division of the amplitude by the distance is meaningless. However, we accept this incorrectness in Fig. 11 because the differences and residuals rather than the variations are the important parameters for our discussion.

The results of the cumulative binning are shown in Fig. 10 and 11. The residuals used in generating Fig. 10 and 11 are the "cleaned" ones, obtained after removing the perturbations listed in Tables 7 and 8 (see also discussion of Fig. 8a–h). Fig. 10a–c refers to the 1997 (Montecristo) sea trial, Fig. 11a–e to the 1996 (Ligurian coast) sea trial. Each page shows data from a particular pair of OBMs. Each vector component and each diurnal interval occupies one panel on the page. The number of events per hour (more precisely, their decadic logarithm) is displayed using different colors for the variations, the differences, and the residuals.

Fig. 10 and 11 may be used in the following way: For a selected pair of magnetometers (which means basically a specific geographic location), one refers to the

corresponding page. For a selected diurnal interval (out of four possible) and a selected magnetic field component (X, Y or Z), one looks up the corresponding panel. For a selected sensitivity threshold (in units of nT and nT/km, respectively), one finds in the panel the log-scaled frequency (in events per hour) of the magnetic field differences and residuals exceeding the specified threshold.

Qualitatively, nothing new is learned from Fig. 10 and 11 when confronted with Fig. 8. Quantitatively, the following type of statements can be made. The upper left panel of Fig. 10a may serve as a first example. Let us assume that magnetic field measurements were made every day but only between 04:30 and 09:30 UTC, with two properly operating OBMs, 17 and 19. We find the decadic logarithm of the number of events/hour of the X (north) component of the magnetic field variation of OBM 17 to be about -0.7 at 1.3 nT bin size, +0.15 at 0.8 nT bin size, and as much as +1.05 at 0.4 nT bin size. This component could thus be expected to pass once every 5 hours a level of ±1.3 nT, once every 40 minutes a level of ±0.8 nT, and about every 5–6 minutes a level of ±0.4 nT. The logarithm of the number of events/hour of the X–component of the magnetic field difference between OBMs 17 and 19 is -1.2, i.e. it would exceed ±0.4 nT only once during 16 hours of observations. The X–component magnetic field residual would practically never exceed ±0.25 nT, i.e. it is basically the magnetometer self noise which sets the limit for the residuals.

Fig. 10a can be interpreted in the following way. If the operator of an OBM array residing in the vicinity of Montecristo island would set a detection threshold of ±0.4 nT, the X–component of a single tri–axial magnetometer, even if properly functioning, would issue some 55 false alarms every day between 04:30 and 09:30 UTC. If the X–component difference with a reference magnetometer, 1.1 km away, were considered, the operator would receive a false alarm every three days at most, and if the operator would consider the residual and make sure that he has become aware of all passings of surface vessels, he would never be fooled by a false alarm. Such a statement depends, of course, on the area and the electromagnetic conditions prevailing therein.

To demonstrate this we take Fig. 11a for a second example. As before, we consider only measurements made during the 04:30–09:30 UTC interval and examine only the X–component. All three components of the magnetic field variation of OBM 18 reach several nanoTesla many times per hour and are thus useless for MTB purposes. The difference to the neighbouring sensor, OBM 17, exceeds ±0.74 nT/km once during 4 hours, and ±0.48 nT/km once every 25 minutes. The residual between OBMs 18 and 17 would exceed ±0.35 nT/km once every 12.5 hours but never exceed ±0.48 nT/km. If the operator would set a detection threshold of ±0.48 nT/km, not too different from the one used above, he would receive a false alarm more than twice every hour if he pays attention to the magnetic field difference, but he would practically never receive a false alarm if he used the residual instead. The succeeding diurnal interval, 09:30–18:00 UTC, is much more disturbed. If we consider the same OBM pair and

the same vector component we notice that the difference exceeds a threshold of ±0.74 nT/km every 100 minutes and a threshold of ±0.48 nT/km every 12 minutes. The residual exceeds a threshold of ±0.35 nT/km once every 4 hours and a threshold of ±0.48 nT/km every 19 hours (left panel, second row of Fig. 11a).

Further characteristics of the data can be deduced from Fig. 11. The magnetic field variations are generally larger in the coast–parallel component than in the coast–perpendicular one, and much larger in the vertical component than in the coast–parallel one. The differences and residuals, however, are generally smaller in the coast–parallel component than in the coast–perpendicular one, and still quite large in the vertical component. A magnetometer array operator would thus pay little attention to an alert issued by the vertical component, and most attention to one issued by the coast–parallel component.

This should, however, not be interpreted as an endorsement for the use of two-axis magnetometers. Firstly, the magnetometer resides in an arbitrary attitude on the sea bottom, and all three components are needed in order to realign the vector measurements with a common coordinate system, such as coast–parallel, coast–perpendicular, vertical. Secondly, tests with the magnetic field data used in this report revealed that the residuals of the horizontal magnetic field components become smaller if the vertical component is included in the scheme (trivariate linear regression) as opposed to a scheme which relies exclusively on the horizontal components (bivariate linear regression).

8
Conclusion

We have demonstrated that a local, time–dependent perturbation of the ambient magnetic field, as it is produced by a moving submarine, has to compete with magnetic field fluctuations from other, natural and anthropogenic, sources. The latter are often much more intense than the signal from a passing submarine. The crucial parameter which determines the outcome of the competition is the spatial scale length of the magnetic field perturbations in the bandwidth under consideration.

The bandwidth under consideration is limited by the minimum and maximum time interval a submarine would typically need to traverse the sphere of influence of the magnetic field sensor. This depends on such parameters as the system noise of the sensor, the size of the submarine, and its magnetic treatment. For the Ocean Bottom Magnetometers (OBMs) used at SACLANTCEN, and a medium–sized, untreated submarine, the radius of the sphere of influence would be of the order of 600 metres in the bandwidth used here, 0.0015–0.08 Hz.

If the spatial scale length of the non–submarine magnetic field is larger than that of the submarine magnetic field, a reference technique can be applied which allows to suppress the fluctuations of the ambient magnetic field by comparison with spaced reference sensors. The spatial scale length depends largely on the geographic area where the observations are made. In this report we have discussed data from two different areas, one magnetically very uniform (the Montecristo sea area), the other magnetically highly non–uniform (the Ligurian coastal water).

The Montecristo area can be dealt with in a rather simple way; the spatial correlation between two OBMs is only limited by the noise characteristics of the sensor pair, even over a distance of several kilometres, by far exceeding the submarine sphere of influence. Fig. 8a and 8b demonstrate this by showing that the residual (i.e. the part of the signal that is not linearly correlated between two sensors), is of the order of 0.25 nT, virtually independent of the spacing between the OBMs. In this area, OBMs could be deployed with a *ca.* 1 km spacing which would guarantee that not more than one OBM at a time is subject to the submarine field while all sensors observe practically the same ambient field which can be removed by linear regression or correlation techniques. The Montecristo area is therefore a suitable candidate area for application of the *Remote Reference Technique.*

The Ligurian coastal water is subject to very intense and localized electromagnetic noise, predominantly from a busy coastal railway line. In this area, the spatial uniformity of the ambient magnetic field fluctuations is much poorer than in the Montecristo area. To quantify this, we formed pairs of neighbouring OBMs and computed the magnetic field vector differences and residuals. The residual is that part of the magnetic field fluctuation which is not linearly correlated between the two OBMs and which is therefore not cancelled out when applying a reference technique.

To better assess the diurnal variation ob the anthropogenic magnetic noise, we divided the day into four diurnal intervals with significantly different railway activity (Table 4). We removed all clearly identifiable signatures from passing surface vessels and all obvious sensor spikes and offset jumps from the data and computed magnetic field residuals, using one specific fixed regression matrix for each pair of magnetometers and each diurnal interval. The regression matrices had been determined from a correlation analysis, using the entire data set available, but cleaned for identified ship signatures and anomalous sensor noise such as mentioned above. We then determined how often, for each pair of OBMs, each vector component, and each diurnal interval, the magnetic field variation, difference, and residual would exceed a given threshold. The results are graphically displayed in Fig. 8.

For each pair of neighbouring OBMs in operation during the Ligurian coast sea trial and each magnetic field vector component, the residual was normalized to a hypothetic spacing of 1 km, taking into account the non–normalizable system noise contribution. In other words, we computed the mean spatial gradient of the non–correlated part of the magnetic field fluctuations. We then determined the number of times, averaged over the entire sea trial, which this mean spatial gradient would exceed a given threshold (expressed in nT/km). A complete summary of the results is found in Fig. 11. In order to clearly distinguish a passing submarine from ambient magnetic noise, the occurence frequency of suspicious residuals must be made low, either by setting the threshold high, or by reducing the spacing between magnetometers. An example which shows how to use the results from the previous sections is given in the following.

If, for instance, a magnetometer array operator would set a threshold for the residual of 0.4 nT/km, our results would provide him with the probability of how often he would find this threshold exceeded at each location, without the influence of a submarine or surface vessel. The result, averaged over all days and diurnal intervals of the entire sea trial, is displayed in Fig. 12. The figure shows, for each pair of OBMs (18 17, 19 18, etc.), the number of hours that would typically pass before the residual exceeds the selected threshold. In other words, if the operator considers each time the magnetic field residual passes the threshold a submarine detection event, Fig. 12 provides him with an estimate of the false alarm rate.

Fig. 12 reveals some characteristics part of which we mentioned already in a previous section.
(1) The vertical component of the magnetic field residual exceeds the threshold of 0.4 nT/km several times per hour and can thus be considered irrelevant for submarine detection purposes.
(2) The coast–perpendicular component of the magnetic field residual becomes a more reliable submarine detection parameter the farther away from the coast the OBM pair is located.
(3) The coast–perpendicular component of the magnetic field residual, computed from OBMs having the same distance from the coast (06 → 12 and 04 → 06), has a very low false alarm rate. Hundreds to thousands of hours pass before the threshold is exceeded.
(4) The coast–parallel component of the magnetic field residual is comparable to the coast–perpendicular component when considering pairs with OBMs having different distances from coast (18 → 17, 19 → 18 and 12 → 19), but not when considering pairs having the same distance from coast (06 → 12 and 04 → 06).

An operator tasked with magnetic surveillance of the Ligurian coastal zone would therefore be well advised to heed the following recommendations.

- The vertical magnetic field component has little relevance for submarine detection
- The OBMs should be deployed in such a way that pairs can be formed from OBMs having the same distance from coast.
- In such a case, the coast–perpendicular component of the magnetic field residual yields the best detection parameter.

We emphasize again that these results apply only to the particular area for which the study was made, and to the particular magnetometers used for the measurements. Note that the sensors contribute already 0.25 nT to the hypothetical threshold of 0.4 nT/km. In a different area, the results may be different, as far as the roles of the coast–perpendicular and coast–parallel components are concerned. Close to the coast, the vertical component will always be a poor parameter, for two reasons.
(1) Most of the anthropogenic electric currents flow between different supply points close to the coast, at sea surface level, i.e. they flow horizontally but are impeded by a lateral electrical discontinuity (namely the coast). It is mostly the vertical magnetic field which reflects strongly the horizontal transition from a good conductor to poor conductor.
(2) The coastal effect on electromagnetic induction converts temporal variations of the horizontal magnetic field into vertical variations. As far as magnetic field correlation is concerned, the coastal effect also favours two sites having the same distance from coast over those having different distances from coast.

Thus, a further recommendation to the OBM array operator would be:

- For each area where magnetic surveillance is intended to be established, a few days of magnetic field measurements should be conducted, prior to activating the surveillance system, in order to determine which vector component is best suited and what the false alarm probability is. If the false alarm probability turns out to be unacceptably high, the spacing of the OBMs should be decreased in order to reduce the adverse effect of a large spatial gradient of the residual magnetic field.

Decreasing the spacing has some implication on the reference method chosen. Small sensor spacing (of the order of 1 km or less) requires application of a *Local Reference Technique*, large spacing permits to use a *Remote Reference Technique.*

The difference between the two techniques is demonstrated in Fig. 2 of this report and is here briefly recapitulated. In a *Remote Reference Technique*, only one of the two OBMs forming the pair is influenced by the submarine. Therefore, the residual magnetic field contains its full magnetic signature. In a *Local Reference Technique*, both OBMs of the pair may record a magnetic signal from the submarine (but usually differently), with the effect that the signal is partially correlated between the two OBMs, and the residuals reveal only a fraction of the submarine's magnetic signature.

References

[1] C. E. Barton, "International Geomagnetic Reference Field: The seventh generation", *J. Geomag. Geoelectr.*, **49**, 123–148, 1997.

[2] A. de Santis, C. Falcone, J. M. Torta, "SHA vs. SCHA for modelling secular variation in a small region such as Italy", *J. Geomag. Geoelectr.*, **49**, 359–371, 1997.

[3] G. Schulz, M. Beblo, A. Best, V. Auster, M. Gropius, "Definitive results of the 1992.5 geomagnetic repeat station survey of Germany: Normal field model and anomalies", *Dt. Hydrogr. Z.*, **49**, 21–33, 1997.

[4] Consiglio Nazionale delle Ricerche, "Italy total magnetic field anomaly", ed. E. Pinna, Dipartimento di Scienza della Terra, Pisa, Italia, 1986.

[5] J. Watermann, "The ocean wave dynamo: A source of magnetic ambient noise", SACLANTCEN SR–264, 1997.

[6] R. A. Langel, "The Main Field", in: Geomagnetism, Vol. 1, ed. J. A. Jacobs, pp. 381 ff., 1987.

[7] Hughes Aircraft Company, "Non–acoustic undersea surveillance program — phase 3", Final Report, prepared for NCCOSC, RDT&E Division, 1990.

[8] S. Søvik, "The characterization and recognition of magnetic disturbances caused by the movement of vessels", SACLANTCEN IN–682, 1987.

[9] G. Angenheister, "Registrierung erdmagnetischer Pulsationen, Göttingen 1952/53", *Gerl. Beitr. Geophys.*, **64**, 108–132, 1954.

[10] W. Dammermann, "Eine Apparatur zur Registrierung erdmagnetischer Pulsationen mit Perioden zwischen 0.1 und 10 sec. Aufbau und Messergebnisse", Diploma Thesis, Dept. of Mathematics and Sciences, University of Göttingen, 1966.

[11] E. A. Nichols, H. F. Morrison, J. Clarke, "Signals and noise in measurements of low–frequency geomagnetic fields", *J. Geophys. Res.*, **93**, 13743–13754, 1988.

[12] R. E. Linnington, "The magnetic disturbances caused by DC electric railways", *Prospezioni Archeologiche*, **9**, 9–20, 1974.

[13] P. Palangio, M. Marchetti, L. di Diego, "Rumore elettromagnetico prodotto dalle ferrovie ellectrificate. Effeti sulle misure magnetotelluriche e geomagnetiche", Atti del 10° Convegno Annuale del Gruppo Nazionale di Geofisica della Terra Solida, Roma 6–8 novembre 1991, 745–760, 1991.

[14] J. C. Larsen, R. L. Mackie, A. Manzella, A. Fiordelisi, S. Rieven, "Robust smooth magnetotelluric transfer functions", *Geophys. J. Int.*, **124**, 801–819, 1996.

[15] W. D. Parkinson, "The influence of continents and oceans on geomagnetic variations", *Geophys. J.*, **6**, 441–449, 1962.

[16] P. M. Morse, H. Feshbach, "Methods of Theoretical Physics", McGraw–Hill, 1953, Vol. 1, p. 28

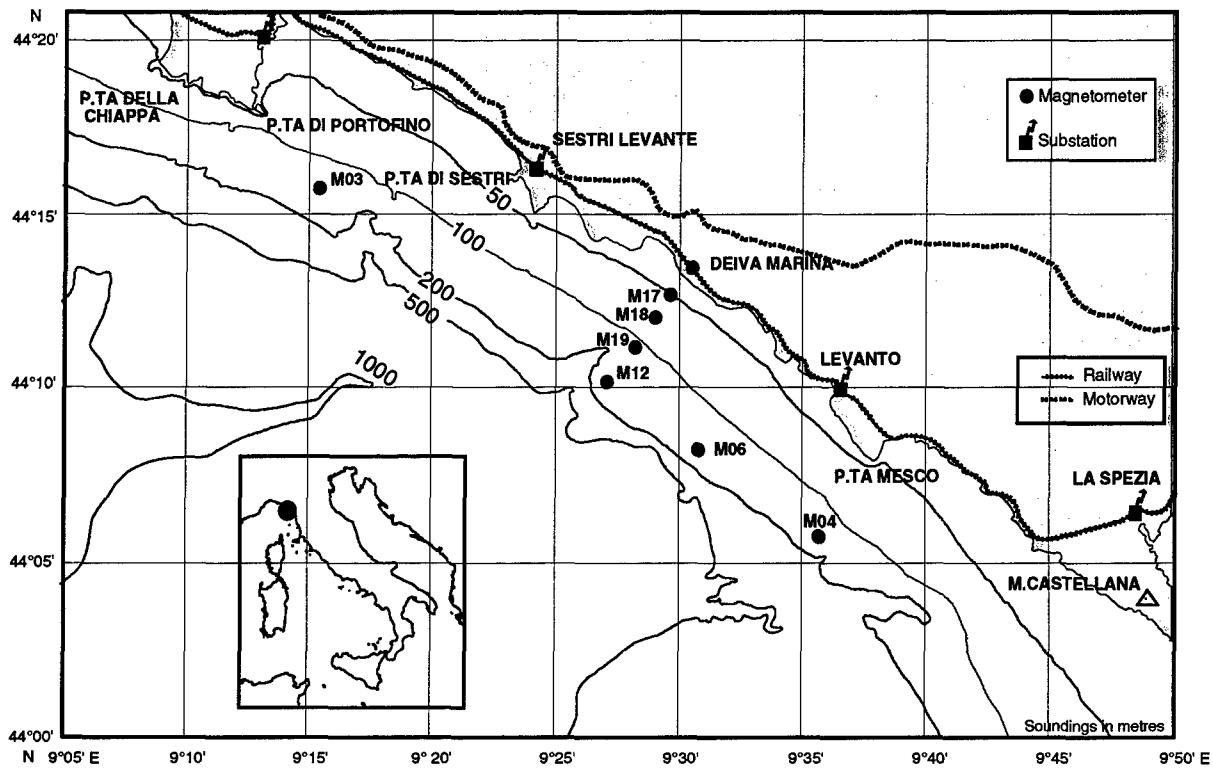

Map 1 *The southern Ligurian coastal one with magnetometer sites marked by black dots. The red dot in the inlay map of Italy indicates the geographic location of the measurement area. Bathymetry in metres.*

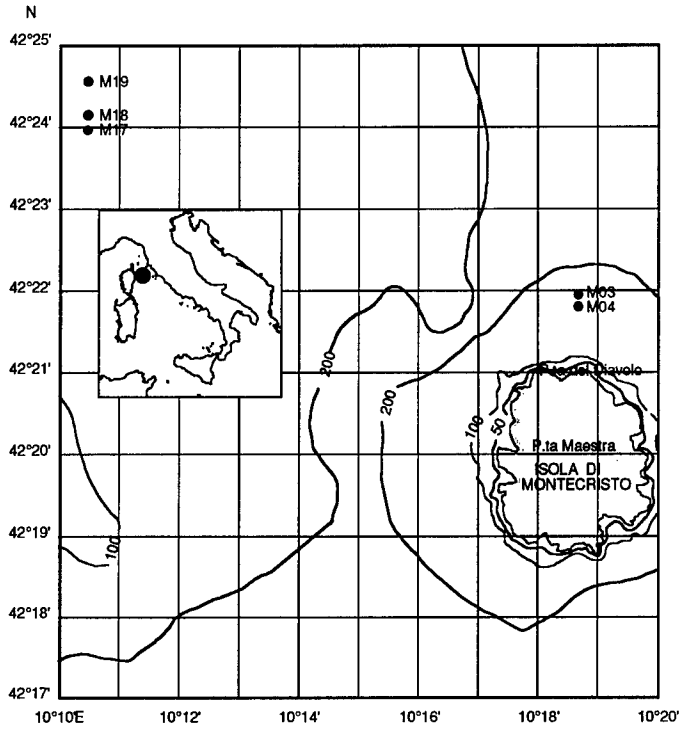

Map 2 *Montecristo island (Tyrrhenian Sea) and its easterly water space, with magnetometer sites marked by black dots. The red dot in the inlay map of Italy indicates the geographic location of the measurement area. Bathymetry in metres.*

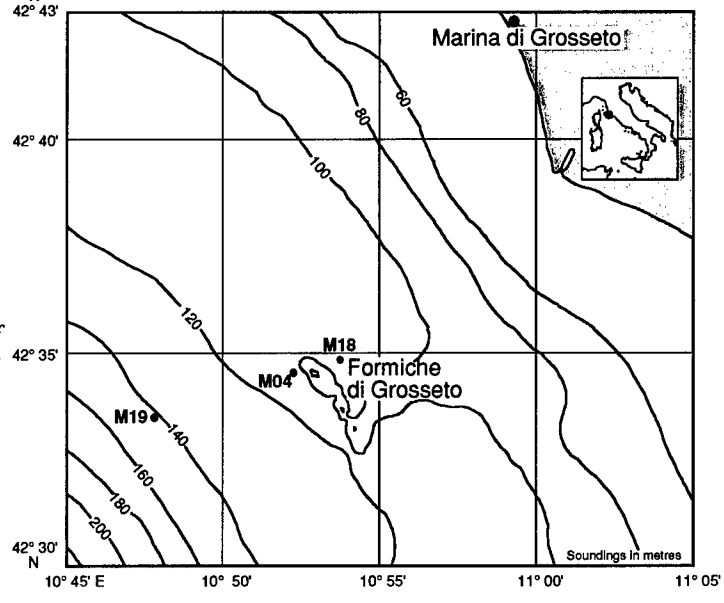

Map 3 *The Formiche di Grosseto area (Tyrrhenian Sea) with part of Tuscany visible in the upper right corner. Magnetometer sites are marked by black dots. The red dot in the inlay map of Italy indicates the geographic location of the measurement area. Bathymetry in metres.*

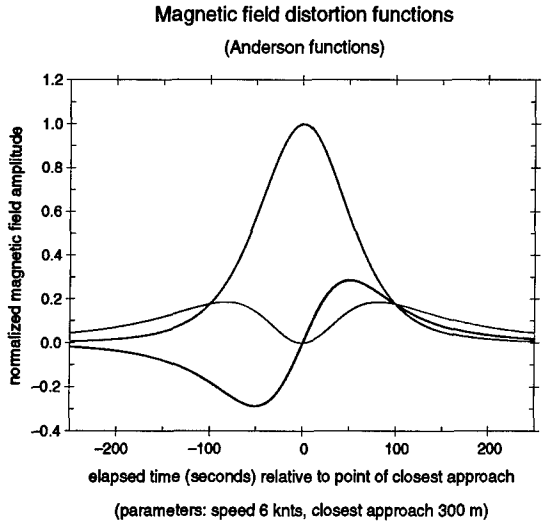

Figure 1 *The magnetic dipole field of a submarine sailing at constant speed along a straight line, as seen by a vector magnetometer at a fixed position, is always and in all its vector components, composed of linear combinations of three simple algebraic functions named "Anderson functions". The coefficients of the linear compositions depend on the dipole strength and orientation, and the ship's velocity, heading, and distance from the magnetometer at the point of closest approach.*

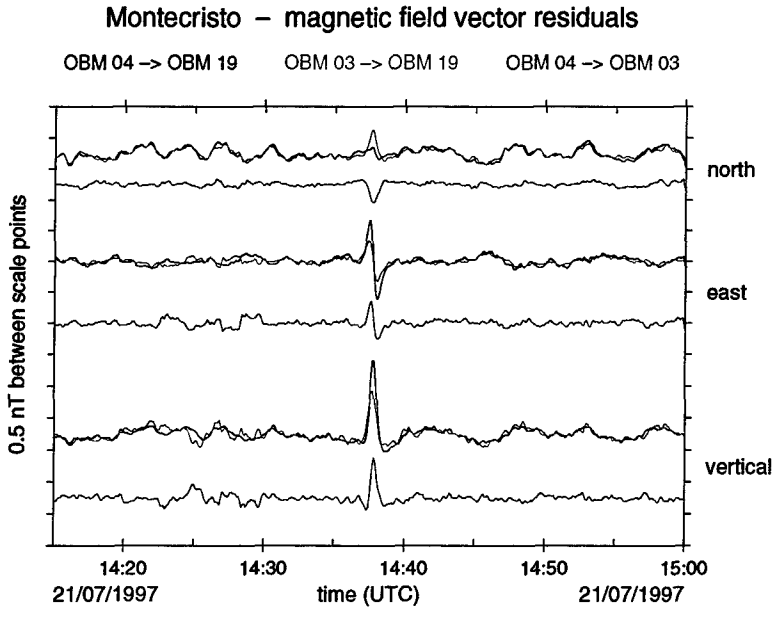

Figure 2 *Magnetic field vector residuals for three pairs of OBMs, 04 –>19, 03 –> 19 and 04 –> 03 (see Map 2 for their positions). The residuals are basically the spatially uncorrelated components of magnetic field variations observed simultaneously at spaced sites. The relatively large excursion at 14:38 UTC marks the passage of the workboat Manning across OBM 04. See the text for further explanations.*

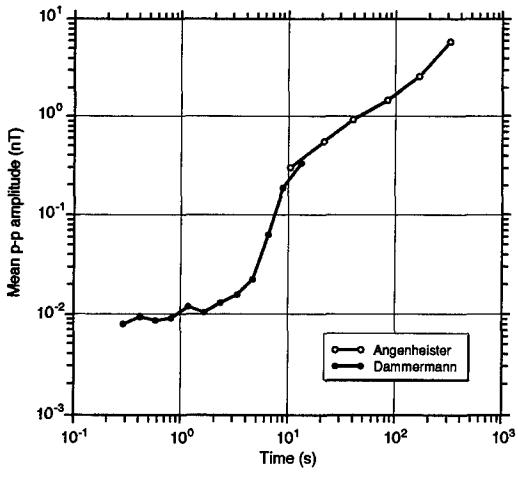

Figure 3 *Mean peak-to-peak amplitudes of natural geomagnetic pc-type variations observed over many years at the Geophysical Institute Göttingen (F.R.G.). Such variations contribute to the always present geomagnetic noise and set a limit to the submarine detection capability if no ambient noise suppression were applied.*

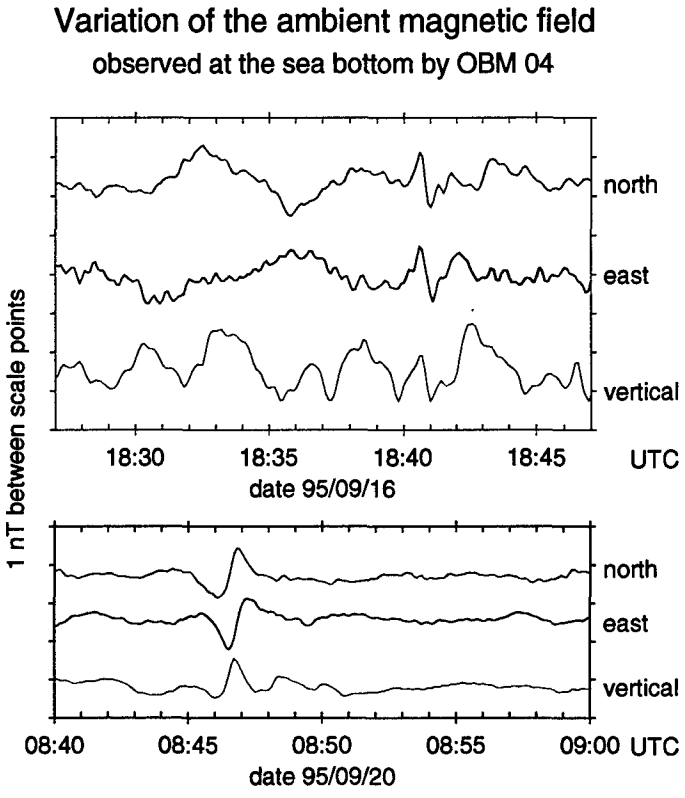

Figure 4a *Temporal variation of the three vector components of the ambient magnetic field on a magnetically moderately disturbed day (upper panel) and a magnetically quiet day (lower panel), recorded with OBM 04 (marked "M04" in Map 3). The highlighted wavelets resemble in shape, amplitude and duration the magnetic field distortion generated by a passing ship (c.f. Figure 1).*

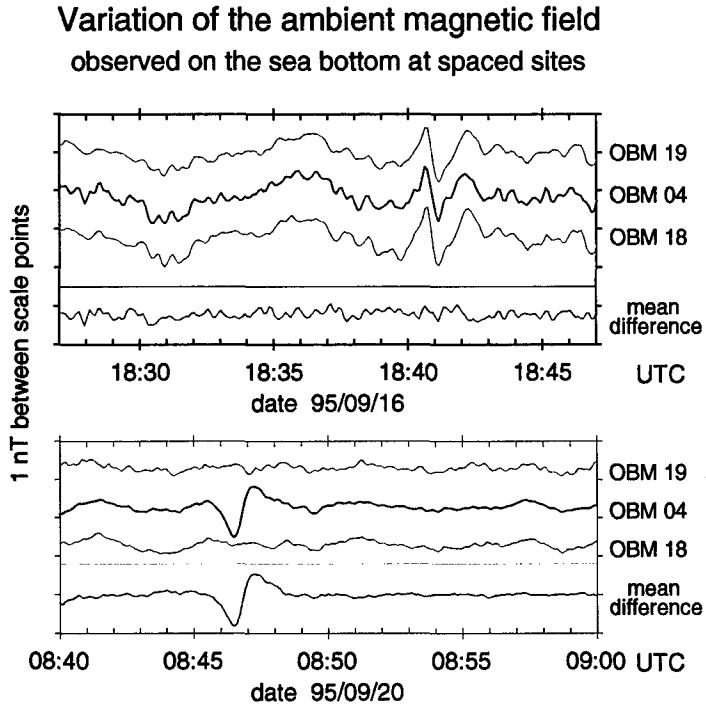

Figure 4b *Variation of the eastward component of the ambient magnetic field recorded simultaneously with three OBMs at spaced sites. The time intervals are identical to those shown in Figure 4a. OBM 18 and OBM 19 were located 2 km eastward and 6 km westward, respectively, of OBM 04 (see also Map 3). The magnetic field difference between OBM 04 and the mean of OBM 18 and 19 (bottom curve in each of the two panels) reveals that the noted wavelets were uniform over several kilometres distance (upper panel) and localized near OBM 04 (lower panel), respectively. The characteristics of the mean difference suggest that the wavelets were of ionospheric origin in the first case (upper panel), and generated by a passing ship in the second case (lower panel), respectively. The northward and vertical components of the magnetic variation were in principle similar to the eastward component and are not shown here.*

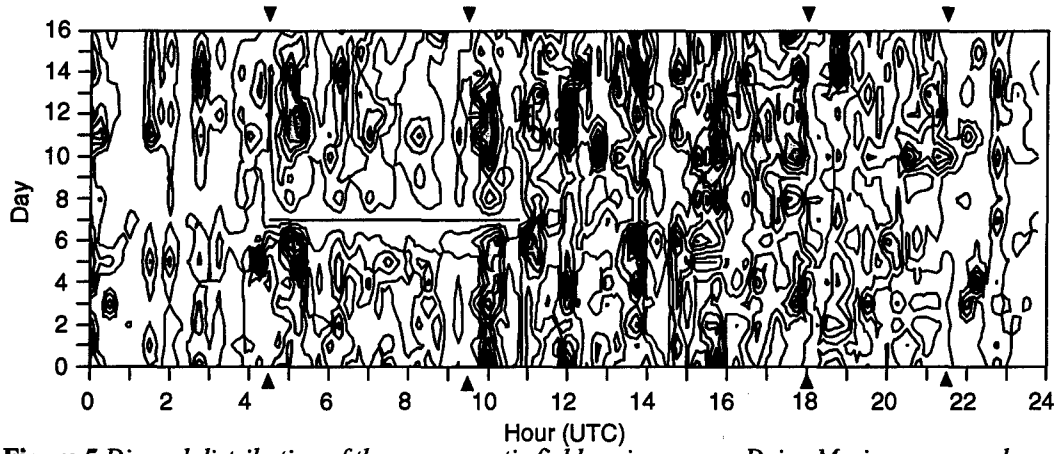

Figure 5 *Diurnal distribution of the geomagnetic field variance near Deiva Marina, averaged over consecutive 15-min intervals. Only relative amplitudes are displayed. The measurements were made continuously over 16 days with a land-based magnetometer operated by A. Magunia (Universität Frankfurt/Main, F.R.G.) at about 500 m distance from the railway line. The small arrowheads along the top and bottom mark the separations we chose in order to break the day into four intervals with different levels of magnetic field variance (c.f. Table 4).*

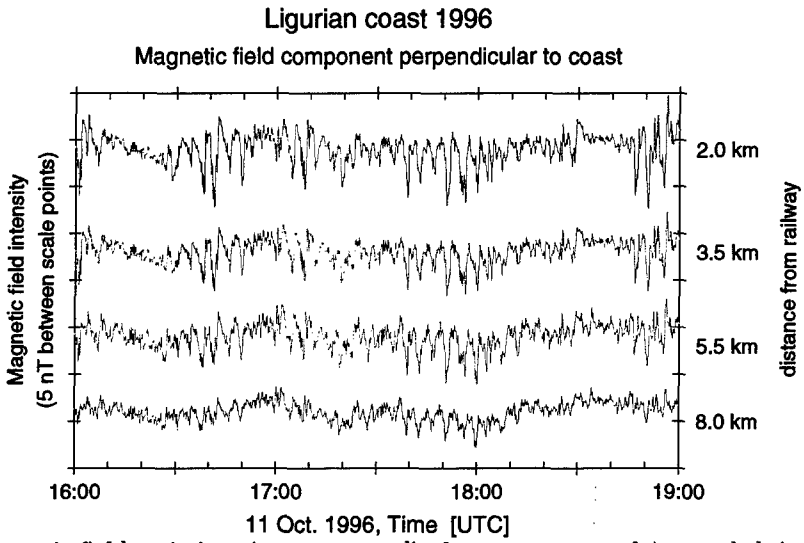

Figure 6 *Magnetic field variations (coast-perpendicular component only) recorded simultaneously by the OBMs 17, 18, 19 and 12, which were aligned along a profile perpendicular to the coast and to a major railway line (which closely follows the coast line), see Map 1. The entire time interval (1600-1900 UTC, equivalent to 17:00-20:00 local time) is strongly affected by train noise which significantly exceeds the ambient magnetic noise from natural sources even at 8 km distance from the railway line. Leakage of electric train currents into the sea is the most likely source of the magnetic noise.*

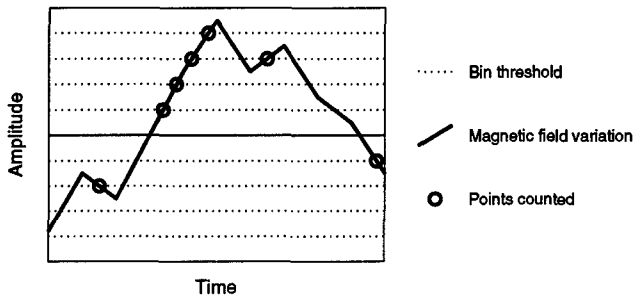

Figure 7 *Schematic of the binning method used to create the distributions presented in Figures 8, 10 and 11. Each time the magnetic field variation, difference, or residual crosses a bin threshold in the direction away from the zero line, the counter is incremented.*

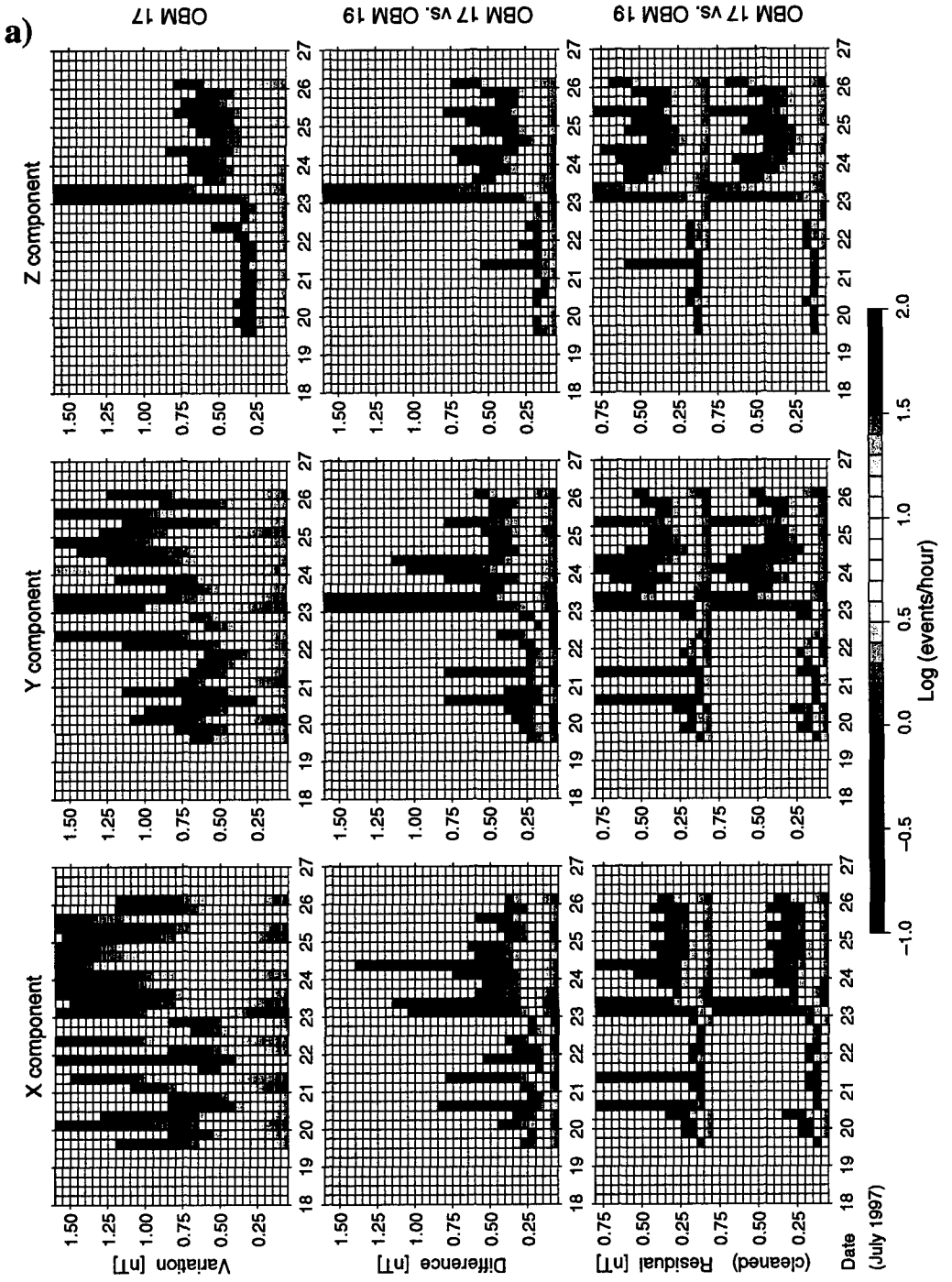

Figure 8 *Occurrence frequency distributions of the magnetic field variations, differences and residuals between two neighbouring tri-axial magnetometers. The OBM identification numbers appear on the right hand side. The logarithmic scale at the bottom relates colour to number of bin threshold crossings per hour ("events/hour"), c.f. Figure 7. The bin thresholds increase along the ordinate, the days (each having four diurnal intervals, c.f. Table 4) along the abscissa. Each residual panel is split into two subpanels, the upper one containing all data, the lower one the data cleaned for identified ship signatures, acoustic interrogation noise, and certain types of sensor noise (see Tables 7 and 8). Figure 8a refers to the 1997 data from the magnetically quiet Montecristo area.*

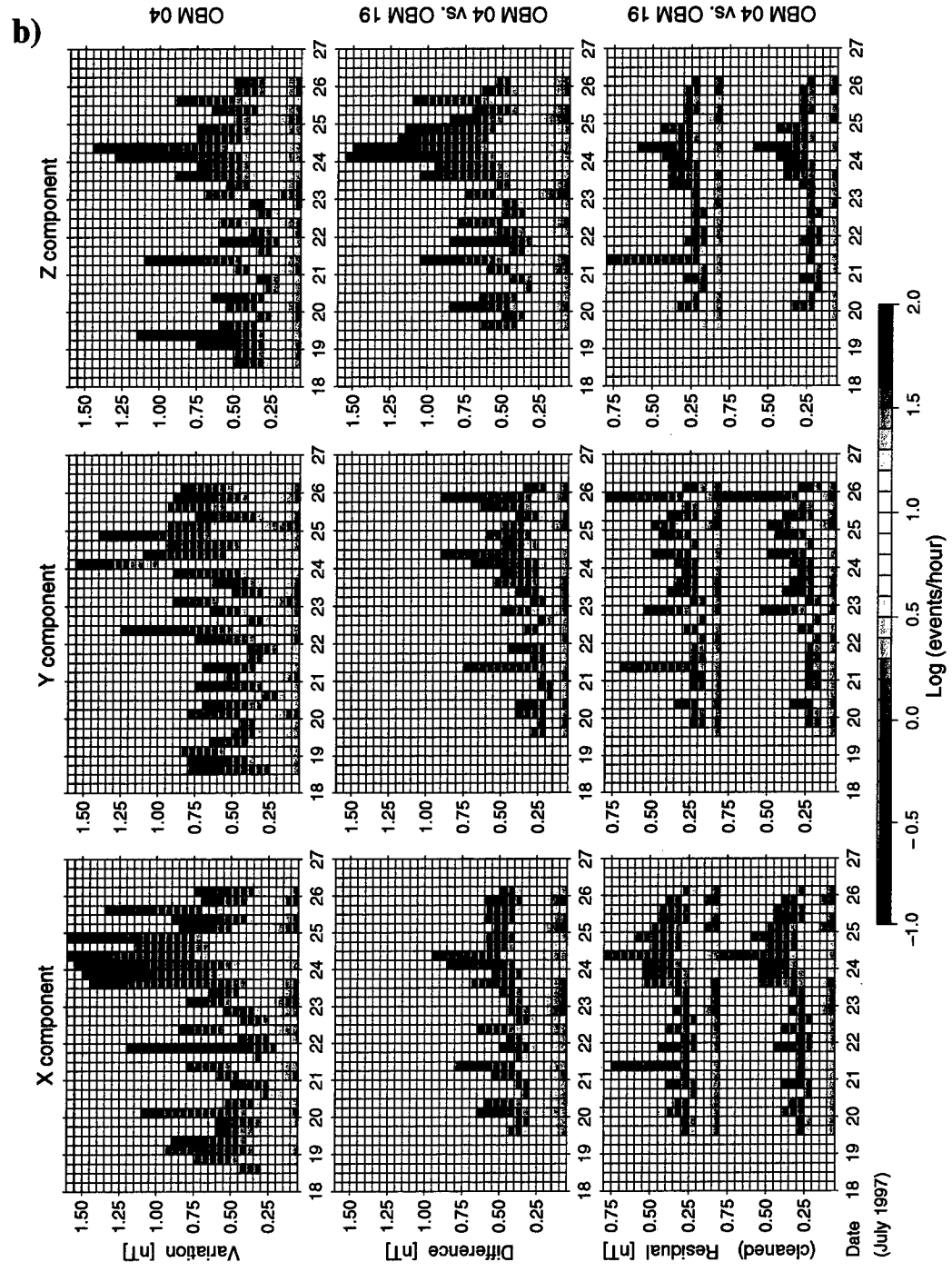

Figure 8 *Occurrence frequency distributions of the magnetic field variations, differences and residuals between two neighbouring tri-axial magnetometers. The OBM identification numbers appear on the right hand side. The logarithmic scale at the bottom relates colour to number of bin threshold crossings per hour ("events/hour"), c.f. Figure 7. The bin thresholds increase along the ordinate, the days (each having four diurnal intervals, c.f. Table 4) along the abscissa. Each residual panel is split into two subpanels, the upper one containing all data, the lower one the data cleaned for identified ship signatures, acoustic interrogation noise, and certain types of sensor noise (see Tables 7 and 8). Figure 8b refers to the 1997 data from the magnetically quiet Montecristo area.*

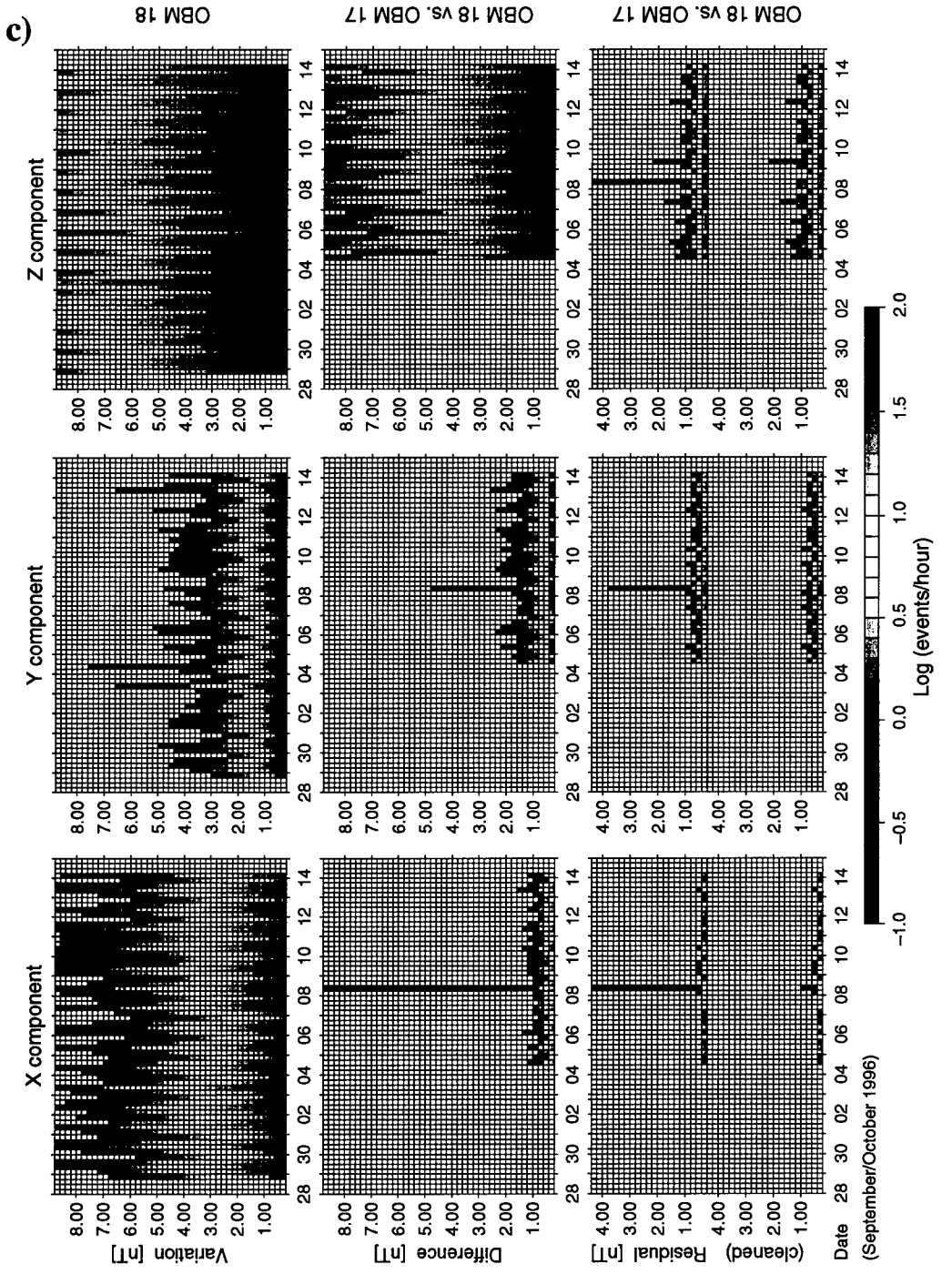

Figure 8 *Occurrence frequency distributions of the magnetic field variations, differences and residuals between two neighbouring tri-axial magnetometers. The OBM identification numbers appear on the right hand side. The logarithmic scale at the bottom relates colour to number of bin threshold crossings per hour ("events/hour"), c.f. Figure 7. The bin thresholds increase along the ordinate, the days (each having four diurnal intervals, c.f. Table 4) along the abscissa. Each residual panel is split into two subpanels, the upper one containing all data, the lower one the data cleaned for identified ship signatures, acoustic interrogation noise, and certain types of sensor noise (see Tables 7 and 8). Figure 8c refers to the 1996 data from the highly disturbed southern Ligurian coastal zone.*

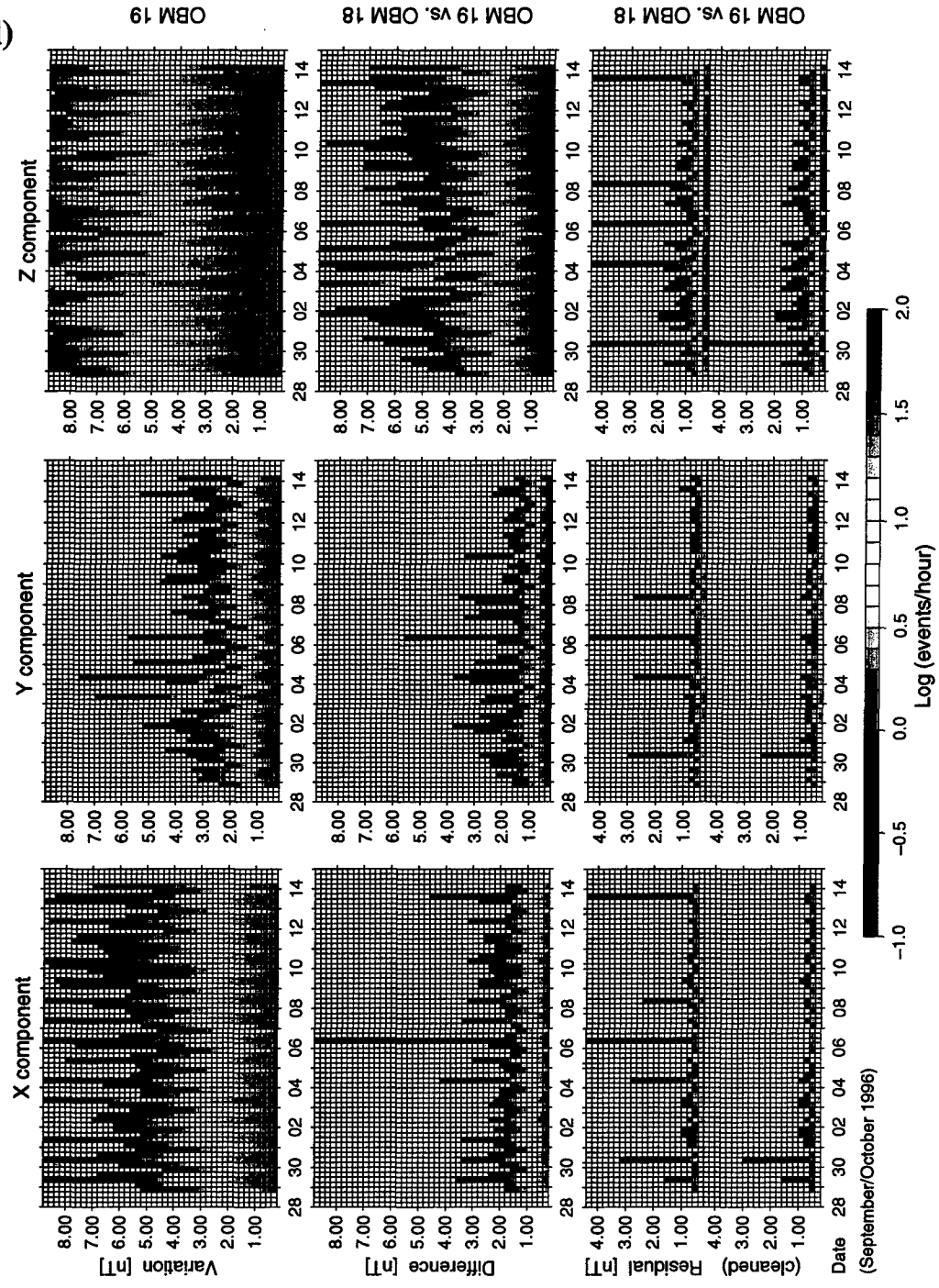

Figure 8 *Occurrence frequency distributions of the magnetic field variations, differences and residuals between two neighbouring tri-axial magnetometers. The OBM identification numbers appear on the right hand side. The logarithmic scale at the bottom relates colour to number of bin threshold crossings per hour ("events/hour"), c.f. Figure 7. The bin thresholds increase along the ordinate, the days (each having four diurnal intervals, c.f. Table 4) along the abscissa. Each residual panel is split into two subpanels, the upper one containing all data, the lower one the data cleaned for identified ship signatures, acoustic interrogation noise, and certain types of sensor noise (see Tables 7 and 8). Figure 8d refers to the 1996 data from the highly disturbed southern Ligurian coastal zone.*

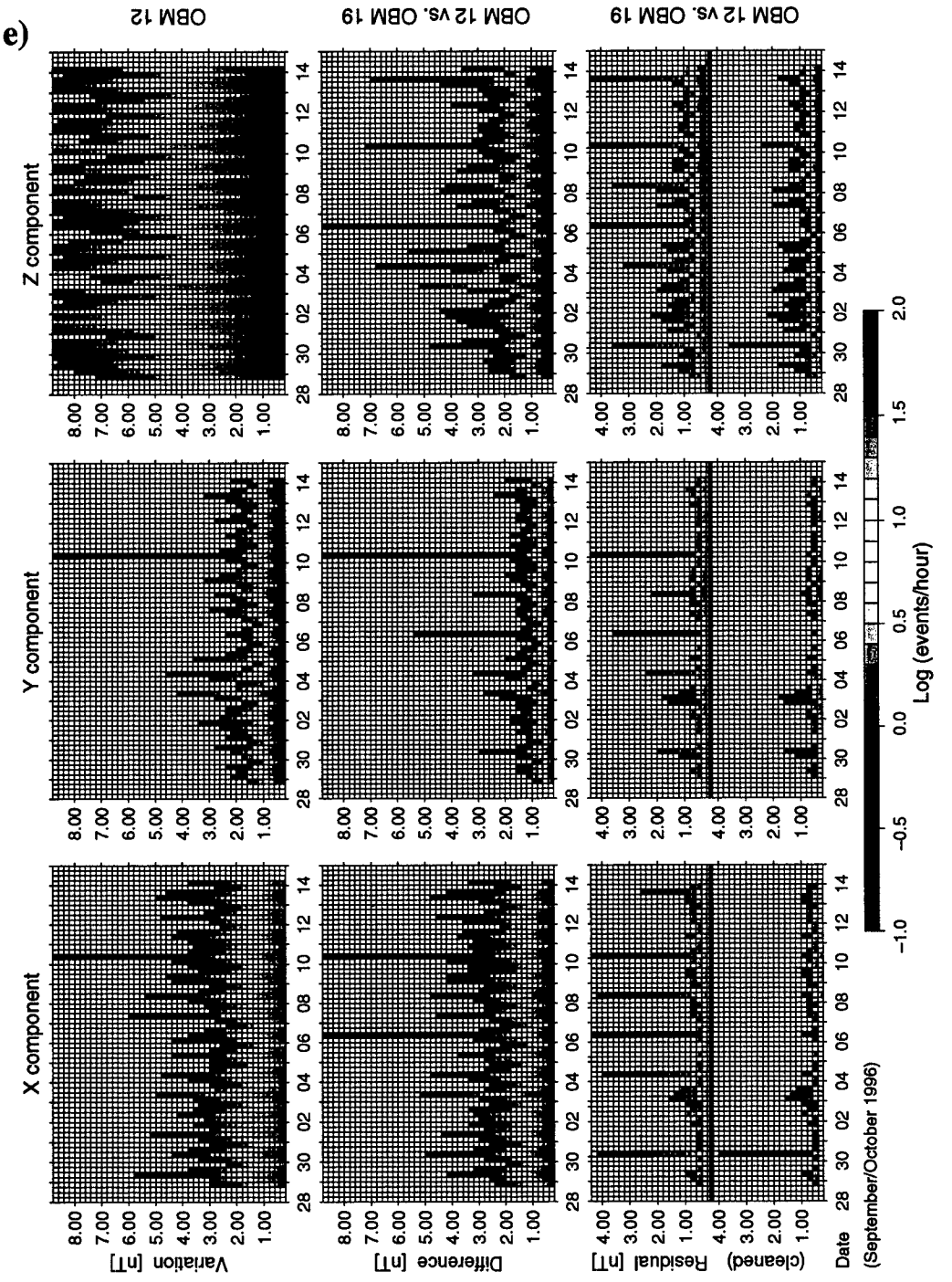

Figure 8 *Occurrence frequency distributions of the magnetic field variations, differences and residuals between two neighbouring tri-axial magnetometers. The OBM identification numbers appear on the right hand side. The logarithmic scale at the bottom relates colour to number of bin threshold crossings per hour ("events/hour"), c.f. Figure 7. The bin thresholds increase along the ordinate, the days (each having four diurnal intervals, c.f. Table 4) along the abscissa. Each residual panel is split into two subpanels, the upper one containing all data, the lower one the data cleaned for identified ship signatures, acoustic interrogation noise, and certain types of sensor noise (see Tables 7 and 8). Figure 8e refers to the 1996 data from the highly disturbed southern Ligurian coastal zone.*

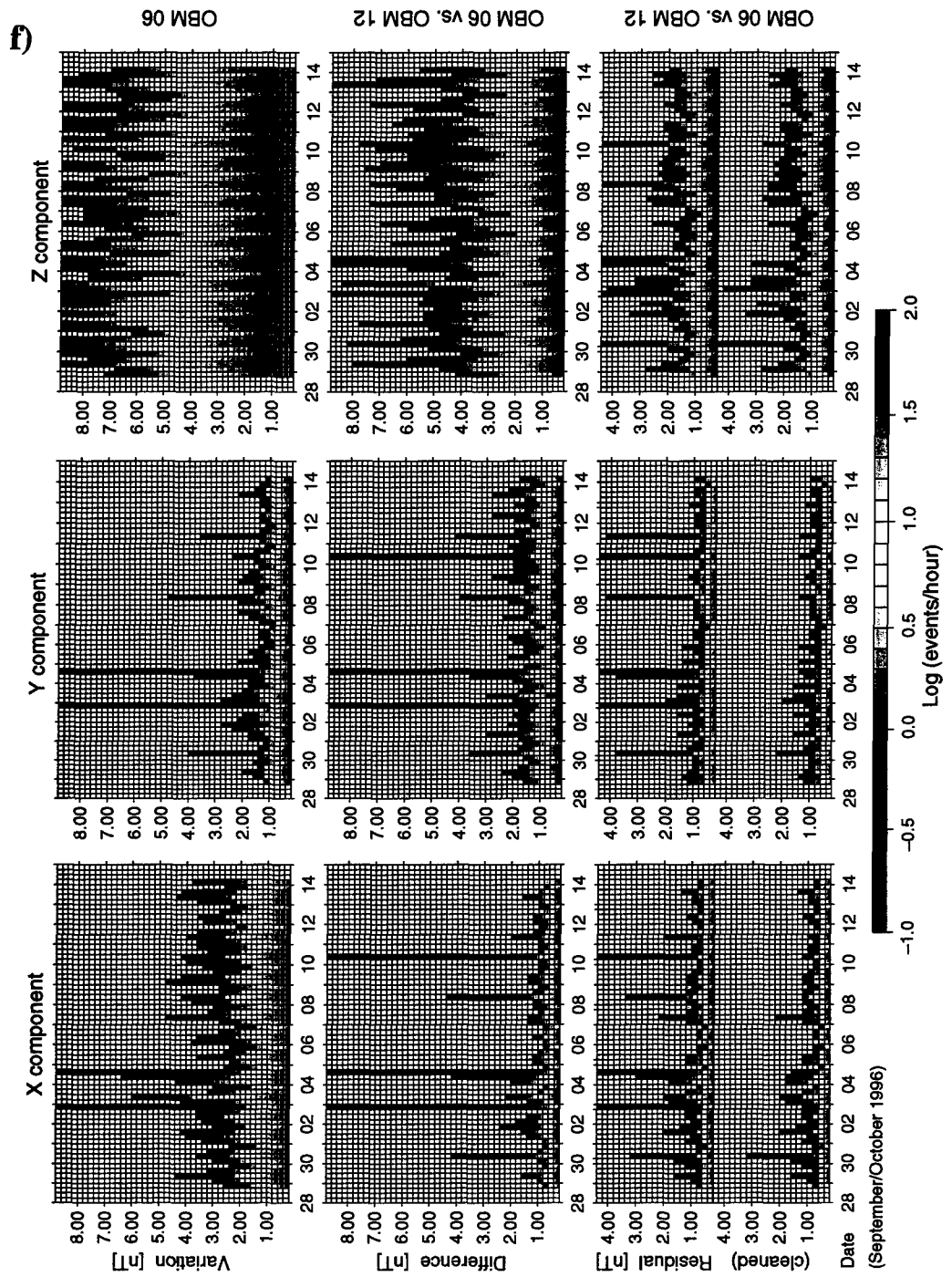

Figure 8 *Occurrence frequency distributions of the magnetic field variations, differences and residuals between two neighbouring tri-axial magnetometers. The OBM identification numbers appear on the right hand side. The logarithmic scale at the bottom relates colour to number of bin threshold crossings per hour ("events/hour"), c.f. Figure 7. The bin thresholds increase along the ordinate, the days (each having four diurnal intervals, c.f. Table 4) along the abscissa. Each residual panel is split into two subpanels, the upper one containing all data, the lower one the data cleaned for identified ship signatures, acoustic interrogation noise, and certain types of sensor noise (see Tables 7 and 8). Figure 8f refers to the 1996 data from the highly disturbed southern Ligurian coastal zone.*

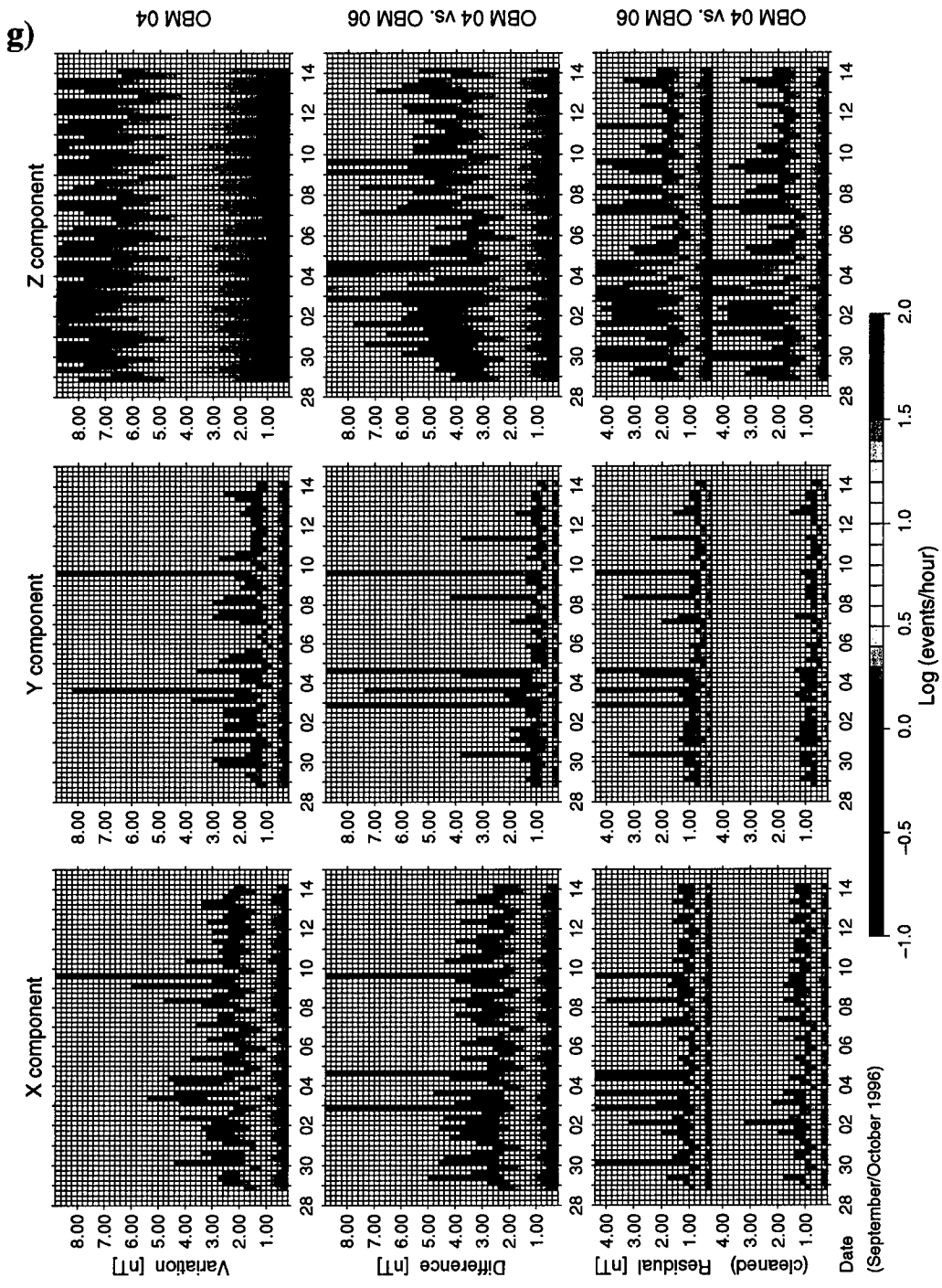

Figure 8 *Occurrence frequency distributions of the magnetic field variations, differences and residuals between two neighbouring tri-axial magnetometers. The OBM identification numbers appear on the right hand side. The logarithmic scale at the bottom relates colour to number of bin threshold crossings per hour ("events/hour"), c.f. Figure 7. The bin thresholds increase along the ordinate, the days (each having four diurnal intervals, c.f. Table 4) along the abscissa. Each residual panel is split into two subpanels, the upper one containing all data, the lower one the data cleaned for identified ship signatures, acoustic interrogation noise, and certain types of sensor noise (see Tables 7 and 8). Figure 8g refers to the 1996 data from the highly disturbed southern Ligurian coastal zone.*

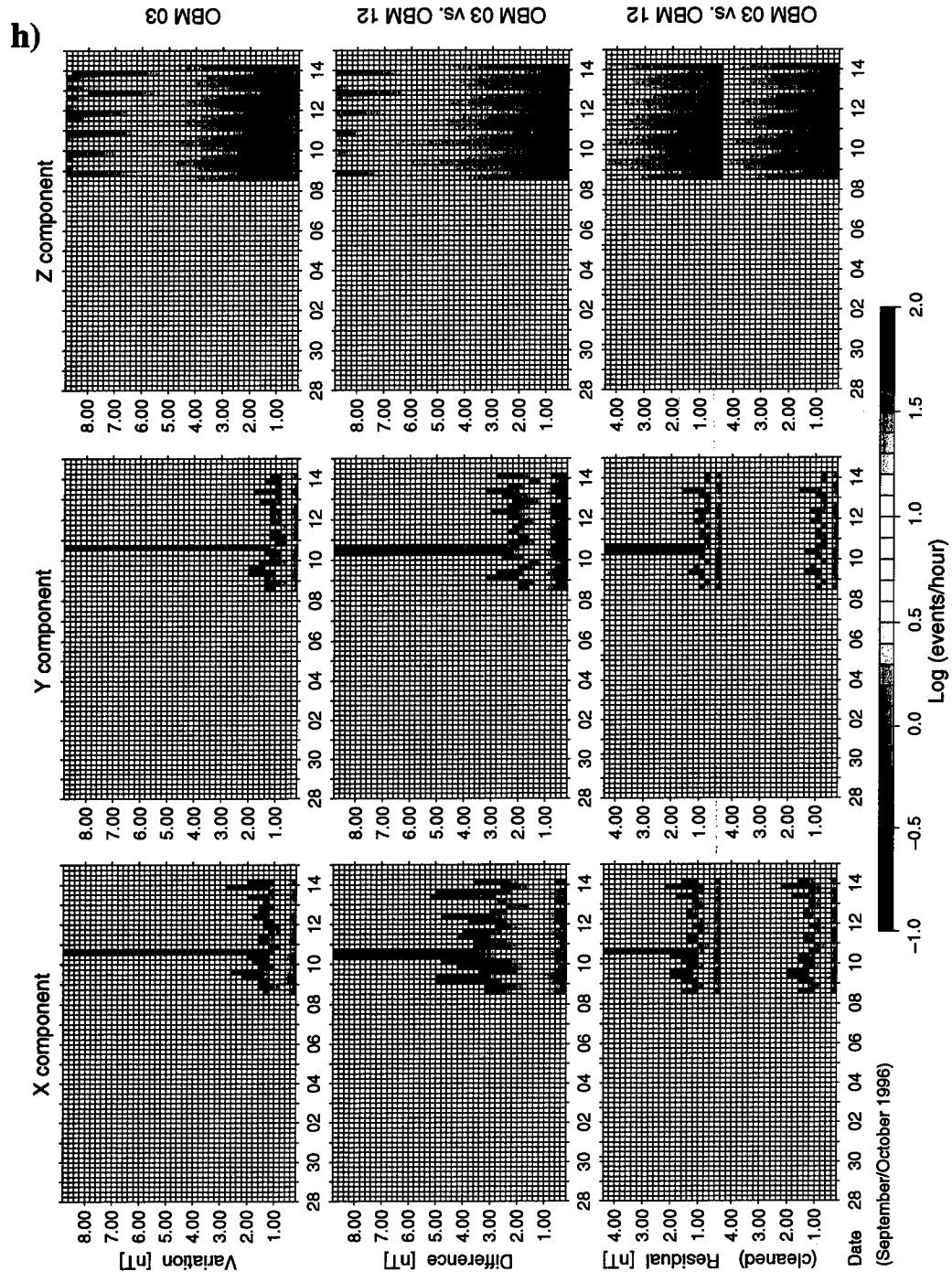

Figure 8 *Occurrence frequency distributions of the magnetic field variations, differences and residuals between two neighbouring tri-axial magnetometers. The OBM identification numbers appear on the right hand side. The logarithmic scale at the bottom relates colour to number of bin threshold crossings per hour ("events/hour"), c.f. Figure 7. The bin thresholds increase along the ordinate, the days (each having four diurnal intervals, c.f. Table 4) along the abscissa. Each residual panel is split into two subpanels, the upper one containing all data, the lower one the data cleaned for identified ship signatures, acoustic interrogation noise, and certain types of sensor noise (see Tables 7 and 8). Figure 8h refers to the 1996 data from the highly disturbed southern Ligurian coastal zone.*

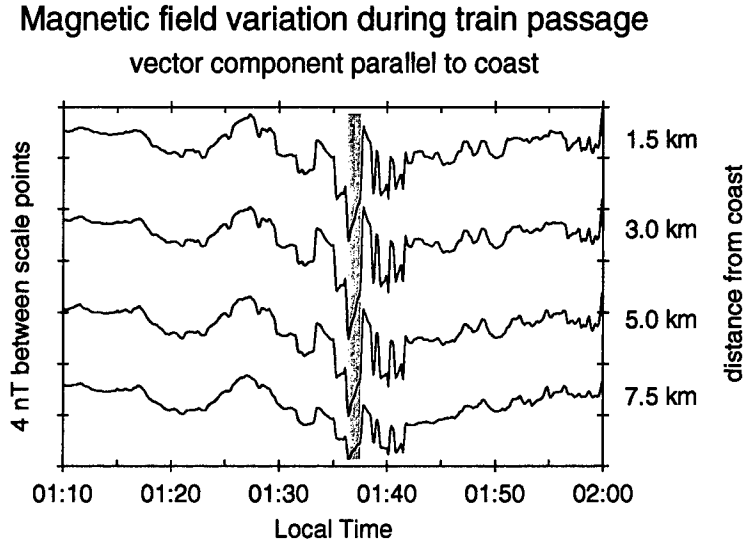

Figure 9 *Variation of the ambient magnetic field (coast-parallel component), measured simultaneously with four OBMs located along a line perpendicular to the coast (modules 17, 18, 19 and 12, see Map 1). The highlighted section marks the passage of a single train on the coastal railway line. Yellow covers the interval when the train was on the rails between the power substations of Levanto and Sestri Levante, green the passing of the train through the railway station of Deiva Marina (without making a stop).*

a)

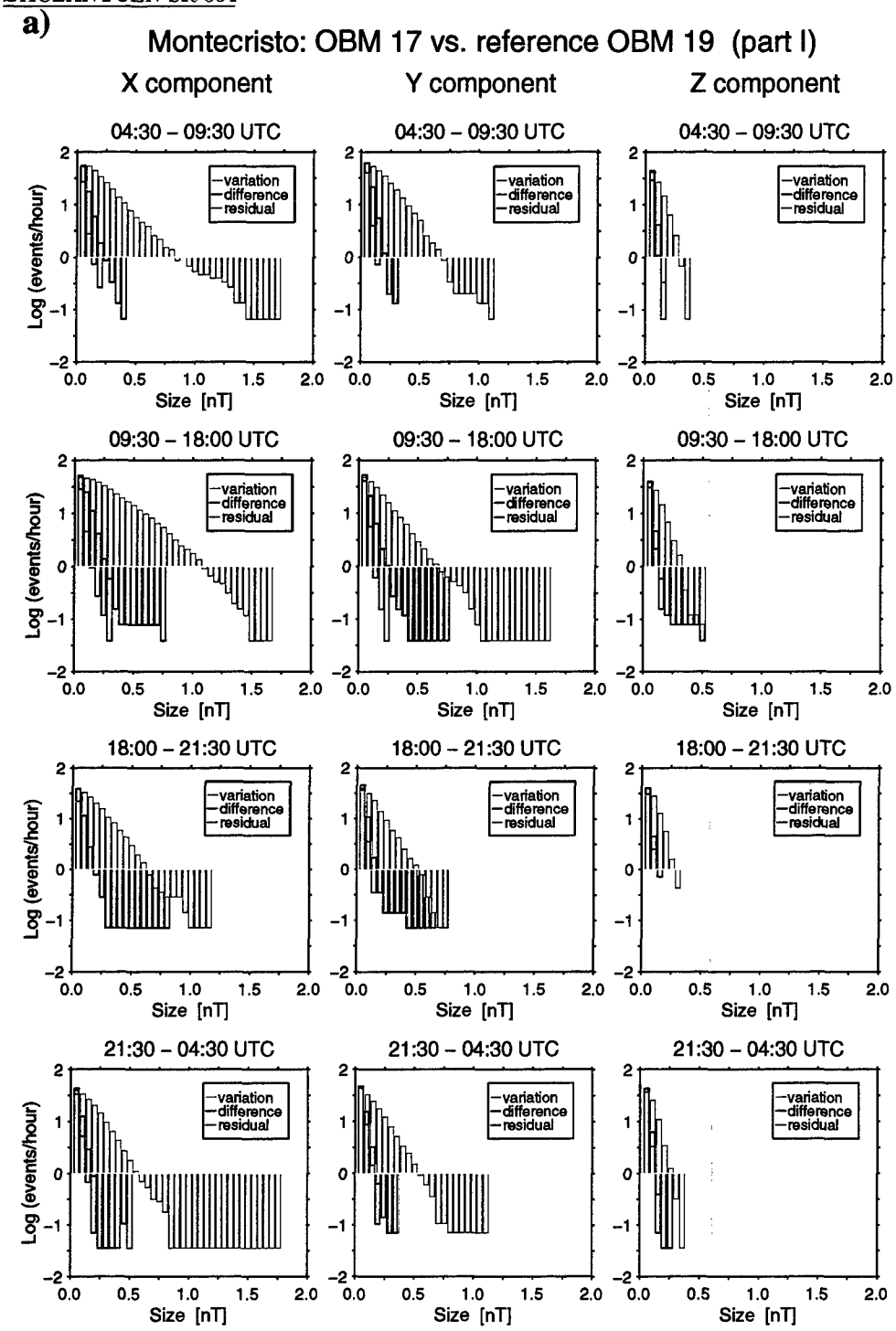

Figure 10 *Cumulative occurrence frequency distributions of magnetic field variations, differences and residuals between two neighbouring sites (1997 data, Montecristo area). Each panel displays the results from a specific vector component and a specific diurnal interval, averaged over the length of the entire sea trial. The term "events/hour" has the same meaning as in Figure 8: The bar diagram indicates how often a certain bin theshold, the size of which increases along the abscissa, is exceeded. The comparison between OBMs 17 and 19 is split into two parts, (I) and (II), in accordance with Figure 8a. 10a contains the data from the first part of the sea trial, up to July 23, and 10b the much noisier data from the second part, starting July 23.*

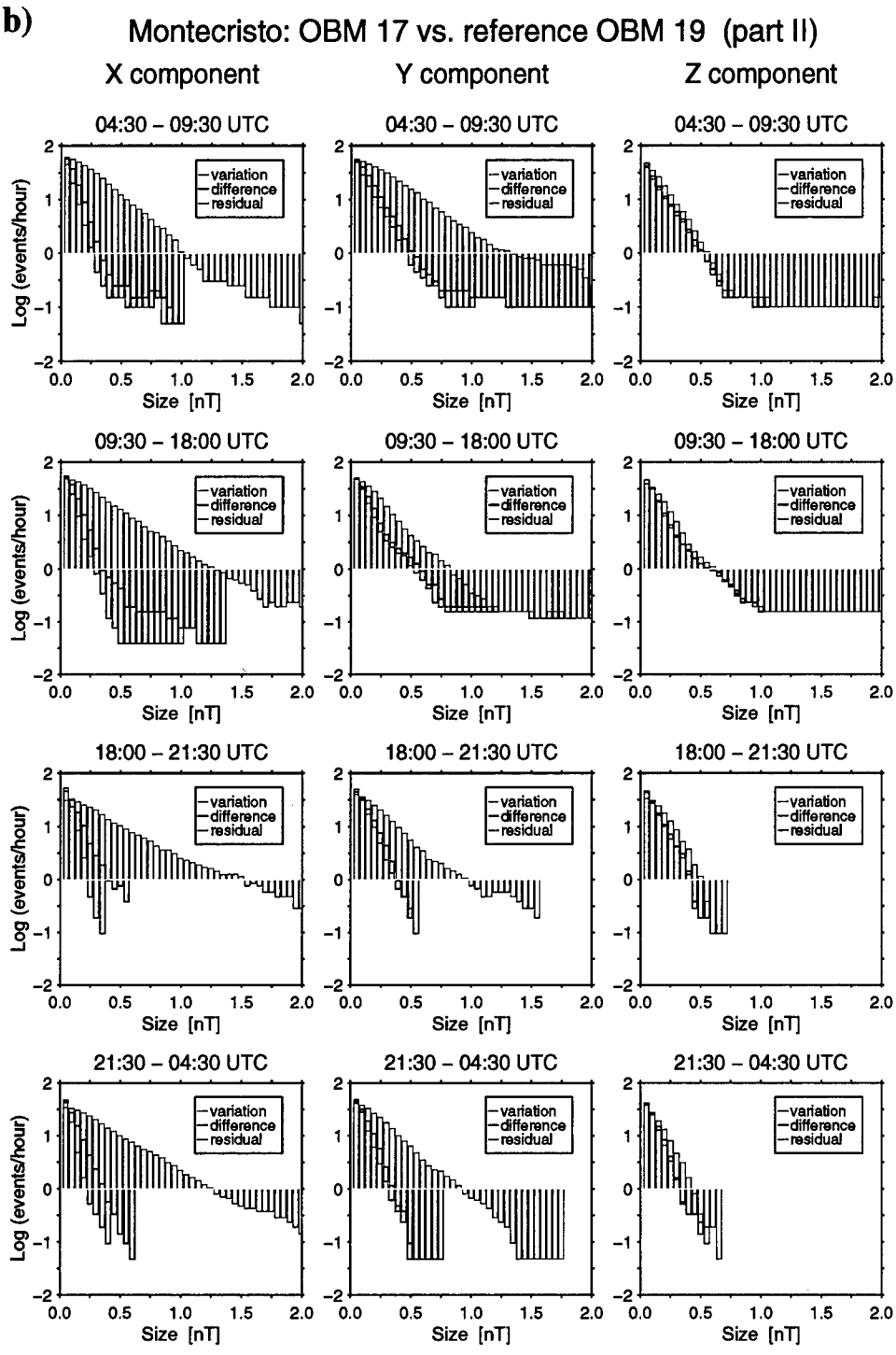

Figure 10 *Cumulative occurrence frequency distributions of magnetic field variations, differences and residuals between two neighbouring sites (1997 data, Montecristo area). Each panel displays the results from a specific vector component and a specific diurnal interval, averaged over the length of the entire sea trial. The term "events/hour" has the same meaning as in Figure 8: The bar diagram indicates how often a certain bin theshold, the size of which increases along the abscissa, is exceeded. The comparison between OBMs 17 and 19 is split into two parts, (I) and (II), in accordance with Figure 8a. 10a contains the data from the first part of the sea trial, up to July 23, and 10b the much noisier data from the second part, starting July 23.*

c)

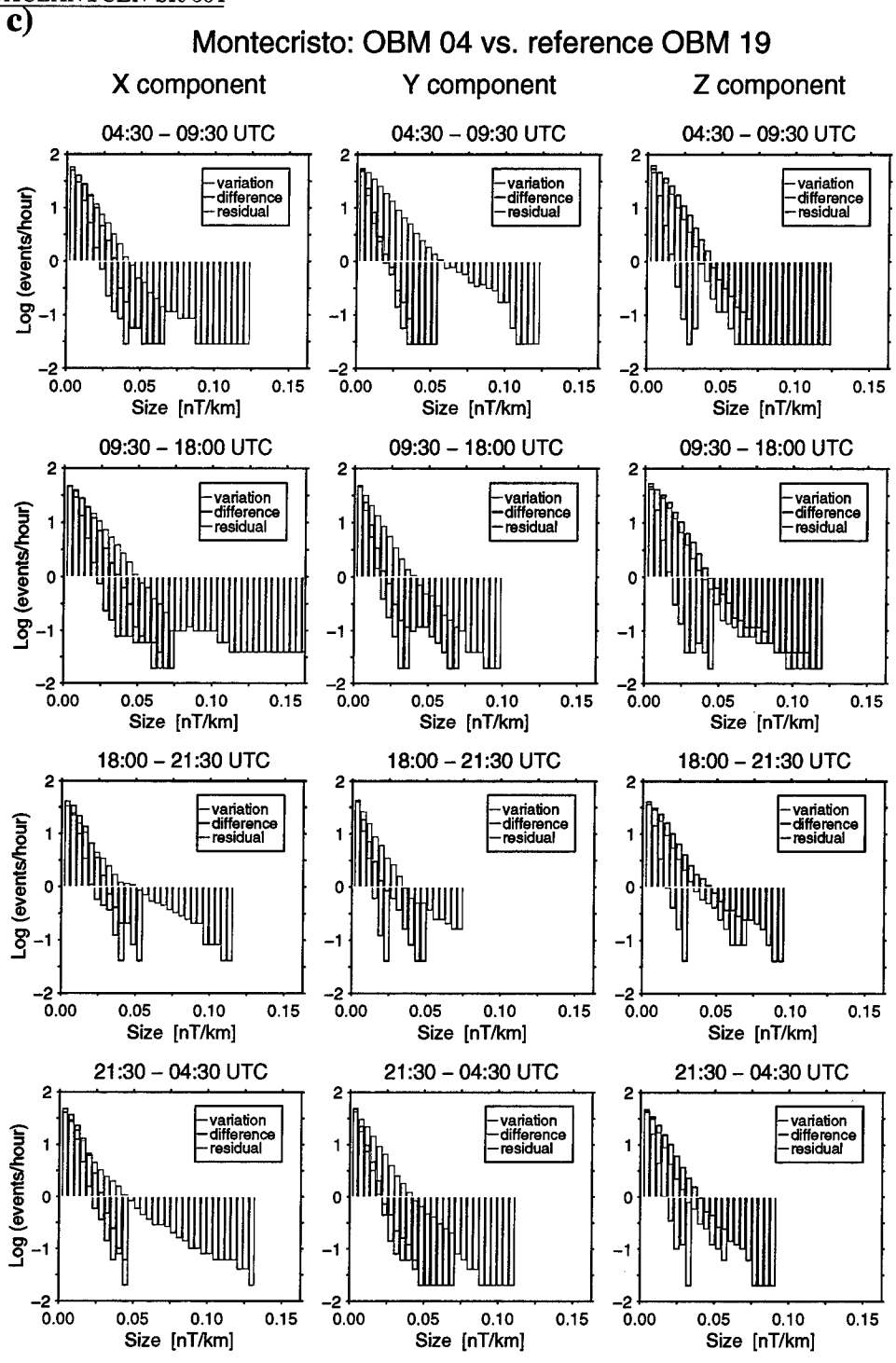

Figure 10 *Cumulative occurrence frequency distributions of magnetic field variations, differences and residuals between two neighbouring sites (1997 data, Montecristo area). Each panel displays the results from a specific vector component and a specific diurnal interval, averaged over the length of the entire sea trial. The term "events/hour" has the same meaning as in Figure 8: The bar diagram indicates how often a certain bin theshold, the size of which increases along the abscissa, is exceeded. The comparison between OBMs 17 and 19 is split into two parts, (I) and (II), in accordance with Figure 8a. 10c covers the entire length of the sea trial*

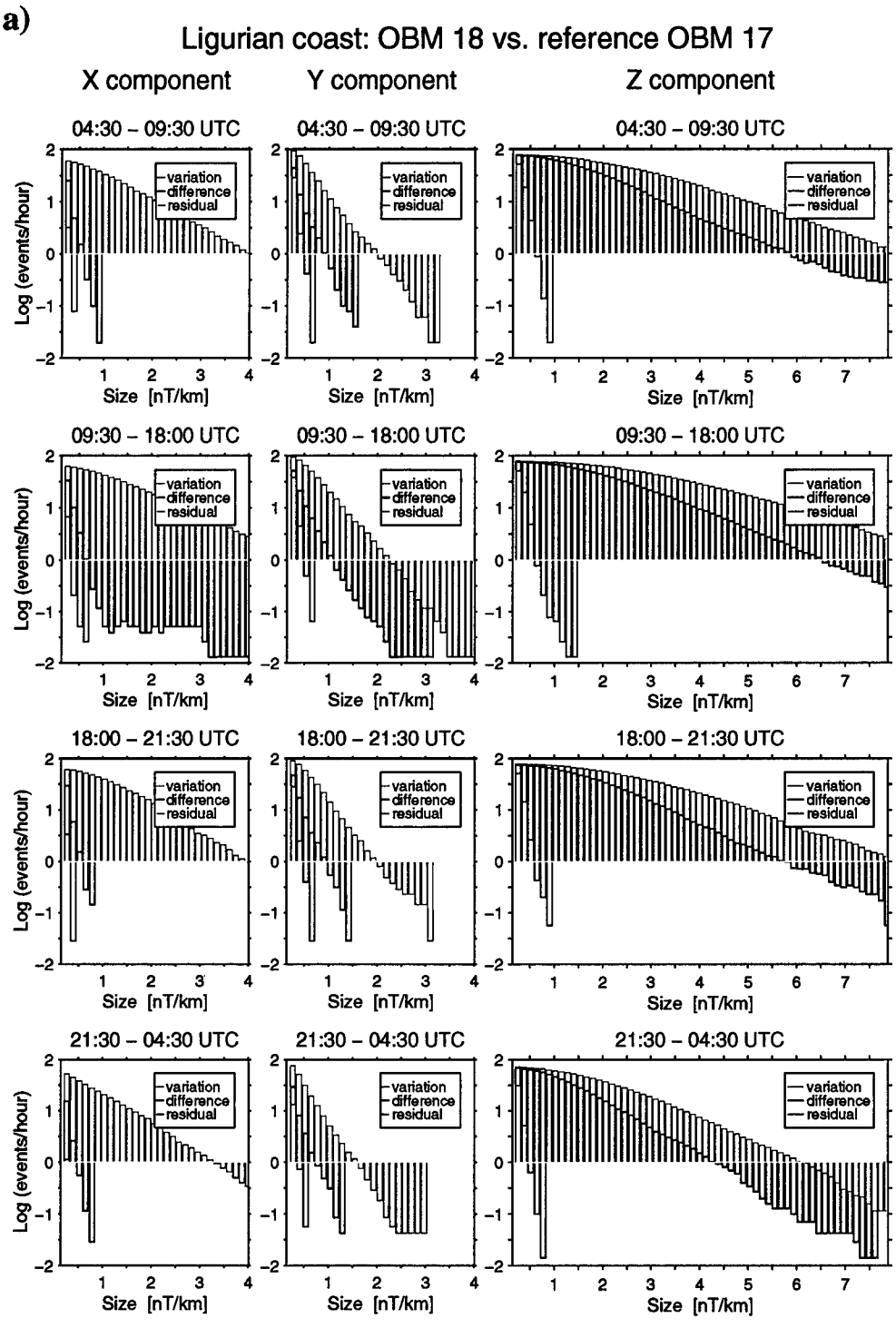

Figure 11 *Like Figure 10 but for the 1996 data (southern Ligurian coast). In this case, the bin sizes were normalized to a hypothetical sensor spacing of 1 km, taking into account the non-normalizable dual-sensor system noise (see Annex D for a detailed discussion). Therefore the abscissa does not start with 0 nT/km but with a certain offset which varies with the distance between the sensors in each pair.*

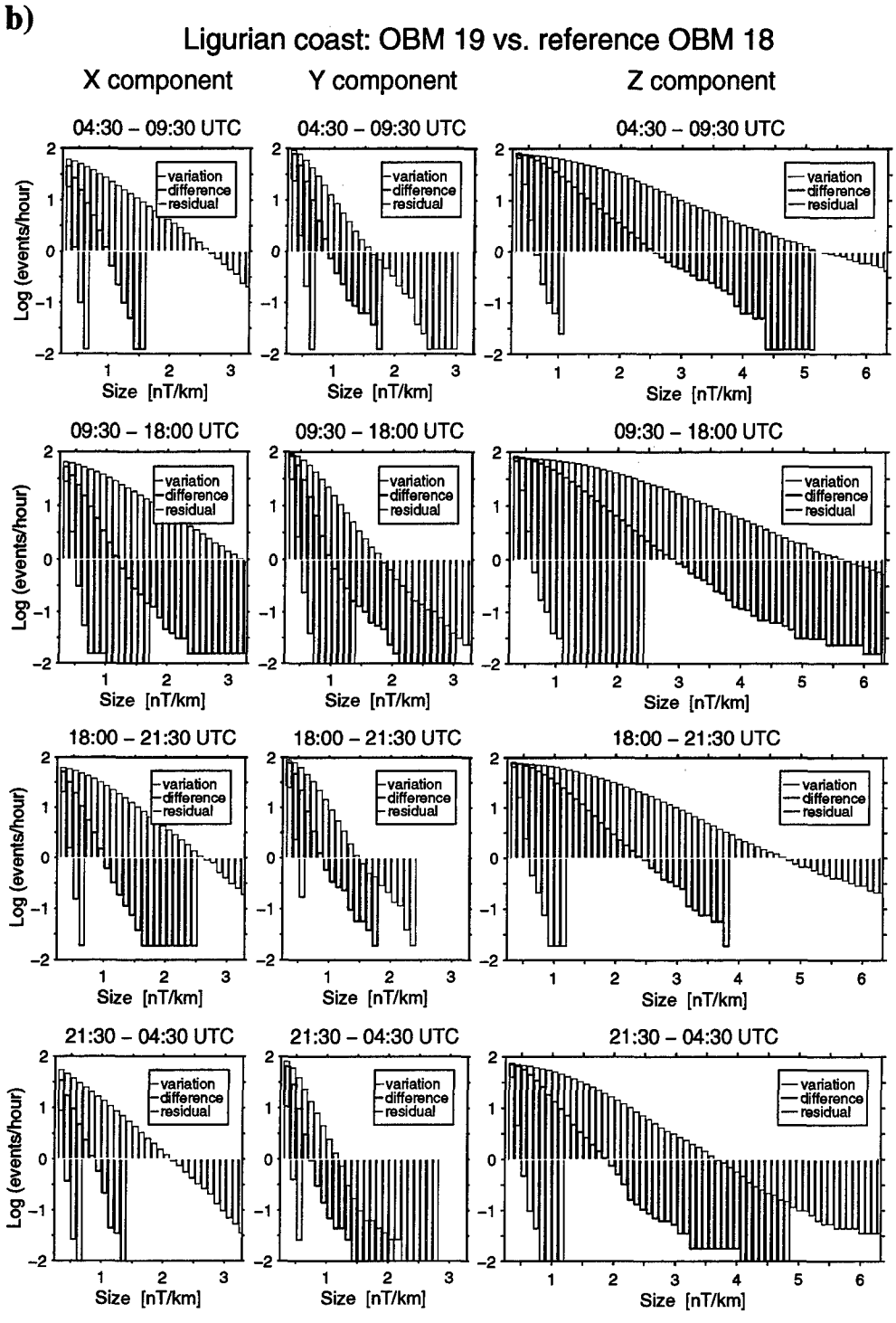

Figure 11 *Like Figure 10 but for the 1996 data (southern Ligurian coast). In this case, the bin sizes were normalized to a hypothetical sensor spacing of 1 km, taking into account the non-normalizable dual-sensor system noise (see Annex D for a detailed discussion). Therefore the abscissa does not start with 0 nT/km but with a certain offset which varies with the distance between the sensors in each pair.*

c)

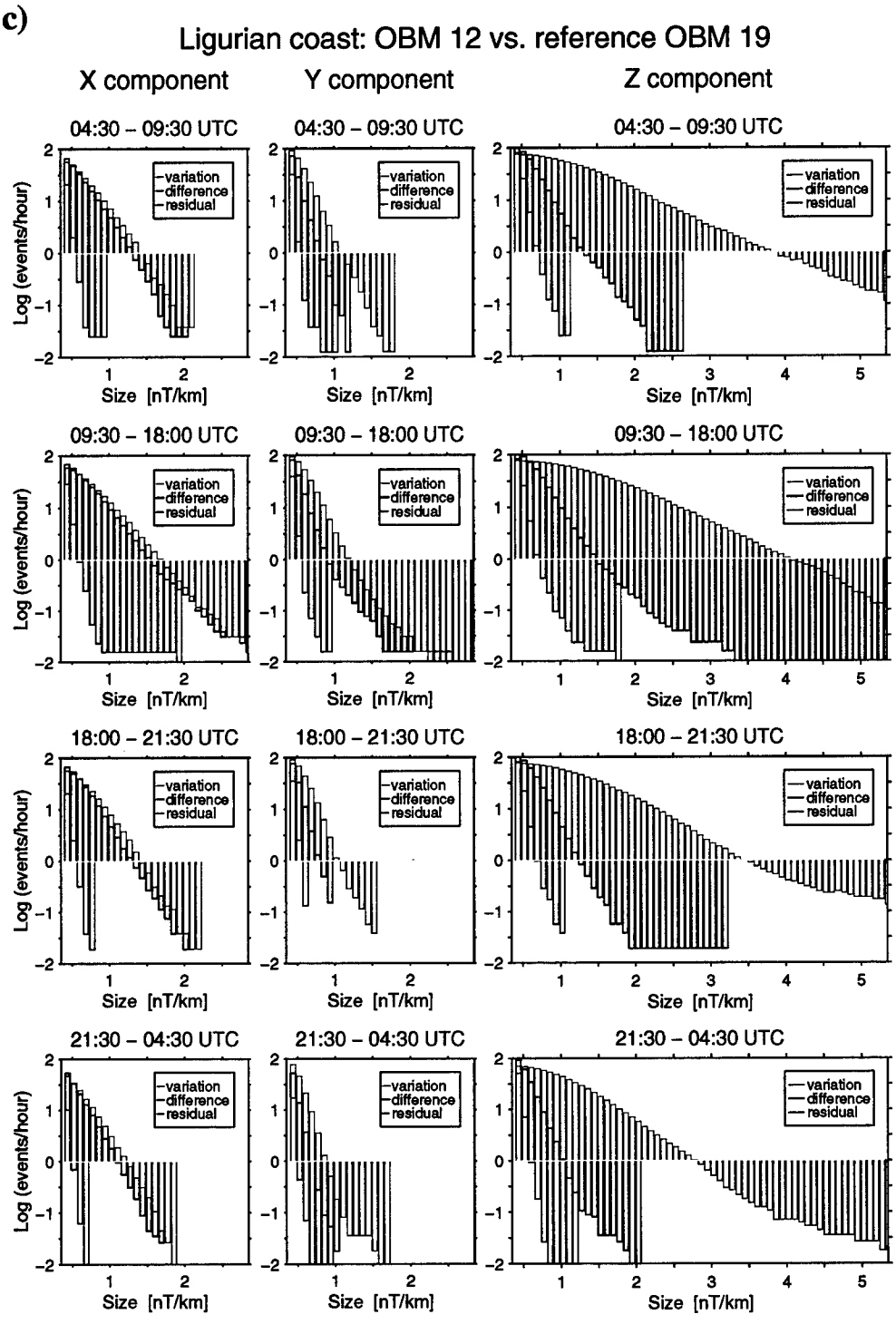

Figure 11 *Like Figure 10 but for the 1996 data (southern Ligurian coast). In this case, the bin sizes were normalized to a hypothetical sensor spacing of 1 km, taking into account the non-normalizable dual-sensor system noise (see Annex D for a detailed discussion). Therefore the abscissa does not start with 0 nT/km but with a certain offset which varies with the distance between the sensors in each pair.*

d)

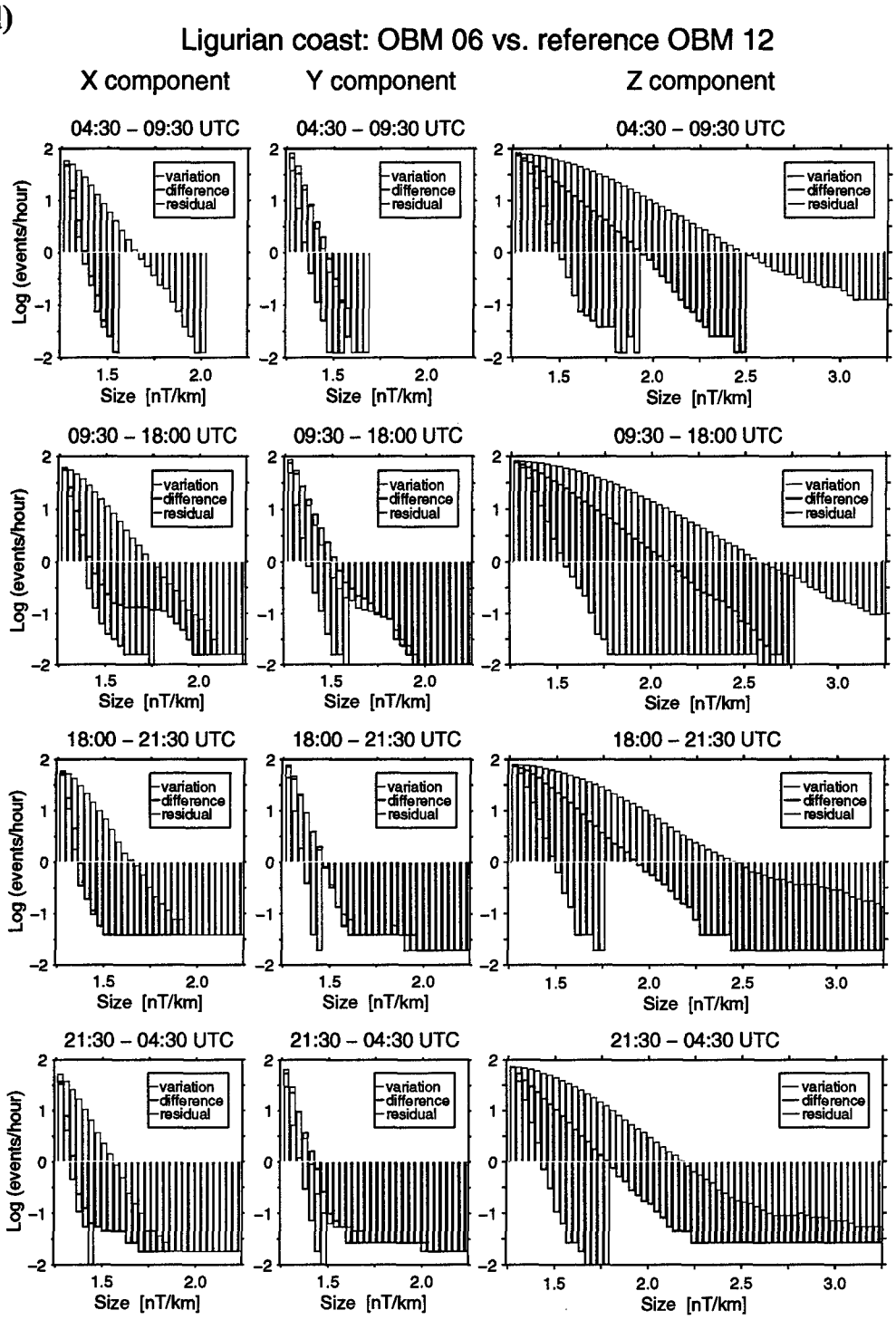

Figure 11 *Like Figure 10 but for the 1996 data (southern Ligurian coast). In this case, the bin sizes were normalized to a hypothetical sensor spacing of 1 km, taking into account the non-normalizable dual-sensor system noise (see Annex D for a detailed discussion). Therefore the abscissa does not start with 0 nT/km but with a certain offset which varies with the distance between the sensors in each pair.*

e)

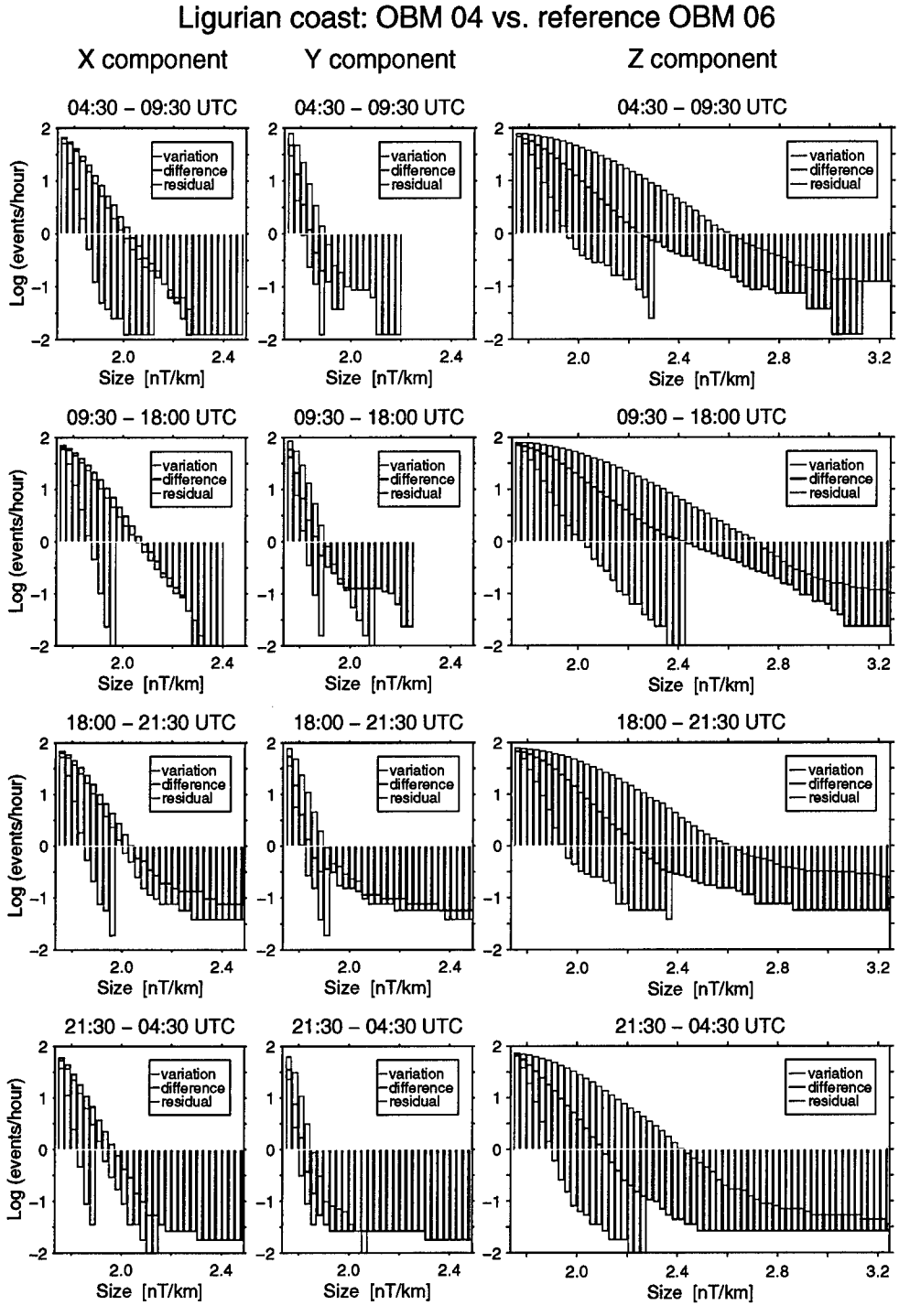

Figure 11 *Like Figure 10 but for the 1996 data (southern Ligurian coast). In this case, the bin sizes were normalized to a hypothetical sensor spacing of 1 km, taking into account the non-normalizable dual-sensor system noise (see Annex D for a detailed discussion). Therefore the abscissa does not start with 0 nT/km but with a certain offset which varies with the distance between the sensors in each pair.*

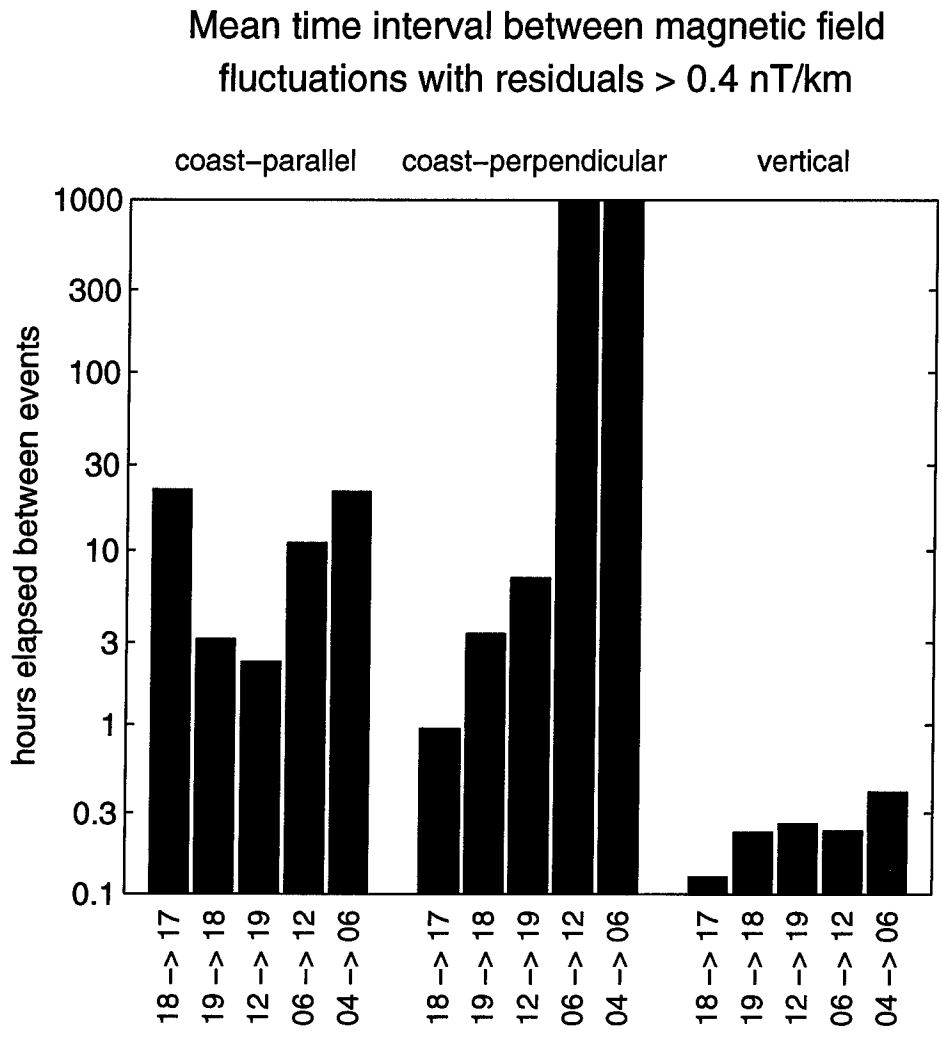

Figure 12 *Mean lifetime of magnetic field residuals between two neighbouring OBMs before they exceed 0.4 nT/km. The relevant OBM numbers are printed along the bottom of the figure. The threshold of 0.4 nT/km includes a distance-independent contribution of 0.25 nT, our estimate of the maximum dual-sensor system noise. The bar diagram suggests short intervals of uninterrupted low residual amplitudes for the vertical magnetic field component and long intervals for residuals between the coast-perpendicular component from two magnetometers at the same distance from the coast.*

Annex A

Transformation of a vector from the magnetometer coordinate system into a geomagnetic coordinate system

Let us assume that the three axes of a vector magnetometer form an orthogonal, right-handed coordinate system defined by the unit vectors $\hat{\mathbf{x}}^{(m)}$, $\hat{\mathbf{y}}^{(m)}$and $\hat{\mathbf{z}}^{(m)}$, aligned with the corresponding sensor axes. It is our objective to find a transformation of the magnetic field variation vector, $\mathbf{B}$, from the $\hat{x}^{(m)}$–$\hat{y}^{(m)}$–$\hat{z}^{(m)}$–system (i.e. the coordinate system in which the components of $\mathbf{B}$ were measured) into a geomagnetic north, east and vertical ($\hat{N}$–$\hat{E}$–$\hat{V}$) coordinate system.

The inclination angles of the $\hat{x}^{(m)}$– and $\hat{y}^{(m)}$–axes against the horizontal plane, θ_x and θ_y, are assumed to have been measured. They are signed positive when the associated axes point upward. The angle between Nadir and $\hat{z}^{(m)}$–axis, θ_z, has not been measured but can be computed from θ_x and θ_y. Specifically, we require that the following constraints apply to the inclination angles

$$\begin{aligned} -\pi/2 < \quad \theta_x, \theta_y \quad &< \pi/2 \\ 0 \leq \quad \theta_z \quad &< \pi/2 \\ \theta_x \neq 0 \quad \bigvee \quad \theta_x &\neq 0 \end{aligned} \tag{A1}$$

Fulfillment of these conditions implies that the magnetometer module is never turned upside down. The heading angle, Δ, measured from the projection of the geomagnetic field vector, $\mathbf{F}$, on the $\hat{x}^{(m)}$–$\hat{y}^{(m)}$–plane, to the magnetometer x–sensor (aligned with the $\hat{x}^{(m)}$–axis by definition), signed positive clockwise around the $\hat{z}^{(m)}$–axis, is assumed to have been recorded as well. If both inclination angles, θ_x and θ_y, were equal to zero, the transformation problem would be trivial and solved by a simple rotation of the $\hat{x}^{(m)}$–$\hat{y}^{(m)}$–plane around the $\hat{z}^{(m)}$–axis by the angle $-\Delta$.

The angles θ_x, θ_y and Δ are occasionally confused with the Euler angles [16], and the latter, in turn, with the attitude angles, pitch, roll and yaw. Euler angles are easy to handle and result in a simple, straightforward transformation scheme. In reality, however, it is rarely possible to measure the Euler angles directly. We will see further below that Euler angles appear also in our algorithm, in fact, our angles θ_z, ψ and φ correspond to the Euler angles Θ,$-\Psi$ and $-\Phi$, in the terminology used in [16]. However, it takes some trigonometric and algebraic manipulation to determine them. This is described in the following.

We define an auxiliary coordinate system based on the unit vectors $\hat{\mathbf{e}}_1$, $\hat{\mathbf{e}}_2$ and $\hat{\mathbf{e}}_3$, in such a way that $\hat{\mathbf{e}}_3$ is pointing vertically down (i.e. $\hat{\mathbf{e}}_3 \equiv \hat{\mathbf{V}}$), $\hat{\mathbf{e}}_1$ is aligned with the projection of $\hat{\mathbf{x}}^{(m)}$ on the horizontal plane, and $\hat{\mathbf{e}}_2$ completes the orthogonal, right-handed system. Note that $\hat{\mathbf{e}}_2$ lies in the horizontal plane but is generally not aligned with the projection of $\hat{\mathbf{y}}^{(m)}$ on the horizontal plane, except for $\theta_x = 0$ or $\theta_y = 0$. The vector $\hat{\mathbf{x}}^{(m)}$ can be represented in the $\hat{e}_1$–$\hat{e}_2$–$\hat{e}_3$–system as

$$\hat{\mathbf{x}}^{(m)} = \begin{pmatrix} \hat{x}_1{}^{(m)} \\ \hat{x}_2{}^{(m)} \\ \hat{x}_3{}^{(m)} \end{pmatrix} = \begin{pmatrix} \cos\theta_x \\ 0 \\ -\sin\theta_x \end{pmatrix} \tag{A2}$$

The first and the second components result from the definition of θ_x, the third from the requirement for unit length, and the "-" sign is required because of the upward orientation of $\hat{\mathbf{x}}^{(m)}$, opposite to $\hat{\mathbf{e}}_3$, when θ_x is signed positive. The vector

$$\hat{\mathbf{y}}^{(m)} = \begin{pmatrix} \hat{y}_1{}^{(m)} \\ \hat{y}_2{}^{(m)} \\ \hat{y}_3{}^{(m)} \end{pmatrix} \tag{A3}$$

is found from the identities

$$\begin{aligned} & & \hat{y}_3{}^{(m)} &= -\sin\theta_y \\ \hat{\mathbf{x}}^{(m)} \cdot \hat{\mathbf{y}}^{(m)} = 0 \quad &\Longrightarrow \quad \hat{y}_1{}^{(m)} &= -\tan\theta_x \sin\theta_y \\ |\hat{\mathbf{y}}^{(m)}| = 1 \quad &\Longrightarrow \quad \hat{y}_2{}^{(m)} &= \pm\sqrt{1 - \sin^2\theta_y \,/\, \cos^2\theta_x} \end{aligned} \tag{A4}$$

In the last equation, only the positive root is valid, otherwise the module would have been turned upsided down. The geometrical constraints on the attitude ensure $\sin^2\theta_y \leq \cos^2\theta_x$. The representation of $\hat{\mathbf{z}}^{(m)}$ in the $\hat{e}_1$–$\hat{e}_2$–$\hat{e}_3$–system is found from

$$\begin{aligned} \hat{\mathbf{z}}^{(m)} &= \hat{\mathbf{x}}^{(m)} \times \hat{\mathbf{y}}^{(m)} \\ &\Downarrow \\ \hat{z}_1{}^{(m)} &= \tan\theta_x \sqrt{\cos^2\theta_x - \sin^2\theta_y} \\ \hat{z}_2{}^{(m)} &= \sin\theta_y / \cos\theta_x \\ \hat{z}_3{}^{(m)} &= \sqrt{\cos^2\theta_x - \sin^2\theta_y} \end{aligned} \tag{A5}$$

From $\hat{z}_3{}^{(m)} = \cos\theta_z$ (by definition) we obtain

$$\begin{aligned} \cos^2\theta_z &= \cos^2\theta_x - \sin^2\theta_y = 1 - \sin^2\theta_x - \sin^2\theta_y \\ \sin^2\theta_z &= \sin^2\theta_x + \sin^2\theta_y \end{aligned} \tag{A6}$$

We recollect the representations of $\hat{\mathbf{x}}^{(m)}$, $\hat{\mathbf{y}}^{(m)}$ and $\hat{\mathbf{z}}^{(m)}$ in the $\hat{e}_1$–$\hat{e}_2$–$\hat{e}_3$–system

$$\hat{\mathbf{x}}^{(m)} = \begin{pmatrix} \cos\theta_x \\ 0 \\ -\sin\theta_x \end{pmatrix} \quad \hat{\mathbf{y}}^{(m)} = \begin{pmatrix} -\tan\theta_x \sin\theta_y \\ \cos\theta_z / \cos\theta_x \\ -\sin\theta_y \end{pmatrix} \quad \hat{\mathbf{z}}^{(m)} = \begin{pmatrix} \tan\theta_x \cos\theta_z \\ \sin\theta_y / \cos\theta_x \\ \cos\theta_z \end{pmatrix} \tag{A7}$$

The inverse transform, namely the representation of the unit vectors $\hat{\mathbf{e}}_1$, $\hat{\mathbf{e}}_2$ and $\hat{\mathbf{e}}_3$, in the $\hat{x}^{(m)}$–$\hat{y}^{(m)}$–$\hat{z}^{(m)}$–system, can be found after a little algebra

$$\hat{\mathbf{e}}_1 = \begin{pmatrix} \cos\theta_x \\ -\tan\theta_x \sin\theta_y \\ \tan\theta_x \cos\theta_z \end{pmatrix} \quad \hat{\mathbf{e}}_2 = \begin{pmatrix} 0 \\ \cos\theta_z / \cos\theta_x \\ \sin\theta_y / \cos\theta_x \end{pmatrix} \quad \hat{\mathbf{e}}_3 = \begin{pmatrix} -\sin\theta_x \\ -\sin\theta_y \\ \cos\theta_z \end{pmatrix} \tag{A8}$$

The unit vector along the projection of $\hat{\mathbf{z}}^{(m)}$ onto the $\hat{e}_1$–$\hat{e}_2$–plane reads

$$\hat{\mathbf{z}}_{\mathbf{p}}{}^{(m)} = \frac{1}{\sin\theta_z} \begin{pmatrix} \tan\theta_x \cos\theta_z \\ \sin\theta_y / \cos\theta_x \\ 0 \end{pmatrix} \tag{A9}$$

and the unit vector $\hat{\mathbf{w}}^{(m)}$, obtained by rotating $\hat{\mathbf{z}}_p{}^{(m)}$ clockwise by $\pi/2$ around the $\hat{e}_3$–axis, reads

$$\hat{\mathbf{w}}^{(m)} = \frac{1}{\sin\theta_z} \begin{pmatrix} -\sin\theta_y / \cos\theta_x \\ \tan\theta_x \cos\theta_z \\ 0 \end{pmatrix} \tag{A10}$$

$\hat{\mathbf{z}}_p{}^{(m)}$ and $\hat{\mathbf{w}}^{(m)}$ are orthogonal vectors, both confined to the $\hat{e}_1$–$\hat{e}_2$–plane. The angle, ψ, between $\hat{\mathbf{y}}^{(m)}$ and $\hat{\mathbf{w}}^{(m)}$, measured positive clockwise from $\hat{\mathbf{y}}^{(m)}$ to $\hat{\mathbf{w}}^{(m)}$, is determined from the following relations

$$\begin{aligned} \cos\psi &= \hat{\mathbf{y}}^{(m)} \cdot \hat{\mathbf{w}}^{(m)} = \sin\theta_x \,/\, \sin\theta_z \\ \sin\psi \cdot \hat{\mathbf{z}}^{(m)} &= \hat{\mathbf{y}}^{(m)} \times \hat{\mathbf{w}}^{(m)} \implies \sin\psi = \sin\theta_y \,/\, \sin\theta_z \end{aligned} \tag{A11}$$

The latter equation follows from the fact that $\hat{\mathbf{y}}^{(m)} \times \hat{\mathbf{w}}^{(m)}$ is (i) perpendicular to $\hat{\mathbf{y}}^{(m)}$, which confines the cross product to the $\hat{x}^{(m)}$–$\hat{z}^{(m)}$–plane, and (ii) perpendicular to $\hat{\mathbf{w}}^{(m)}$ which confines the cross product to the $\hat{z}^{(m)}$–$\hat{z}_p{}^{(m)}$–plane. Both planes have the vector $\hat{\mathbf{z}}^{(m)}$ in common.

We rotate the $\hat{x}^{(m)}$–$\hat{y}^{(m)}$–plane clockwise around the $\hat{z}^{(m)}$–axis by the angle ψ in order to construct a new, right–handed coordinate system based on the orthonormal vectors, $\hat{\mathbf{u}}^{(m)}$, $\hat{\mathbf{w}}^{(m)}$ and $\hat{\mathbf{z}}^{(m)}$, where $\hat{\mathbf{u}}^{(m)}=\hat{\mathbf{w}}^{(m)} \times \hat{\mathbf{z}}^{(m)}$. In the new system, the angle Δ has to be replaced by $\Delta^* = \Delta + \psi$. In the northern hemisphere, the unit vector of the quasi-static geomagnetic field, $\hat{\mathbf{F}}$, points into the halfspace below the horizontal plane. $\hat{\mathbf{F}}$ can be expressed through the northward and downward pointing unit vectors, $\hat{\mathbf{N}}$ and $\hat{\mathbf{V}}$, with the help of the geomagnetic inclination angle, I:

$$\hat{\mathbf{F}} = \hat{\mathbf{N}} \cos I + \hat{\mathbf{V}} \sin I \tag{A12}$$

$\hat{\mathbf{V}}$ can be expressed through a combination of $\hat{\mathbf{z}}^{(m)}$ and $\hat{\mathbf{u}}^{(m)}$

$$\begin{aligned} \hat{\mathbf{V}} &= \cos\theta_z \, \hat{\mathbf{z}}^{(m)} - \sin\theta_z \, \hat{\mathbf{u}}^{(m)} \\ &\Downarrow \\ \hat{\mathbf{F}} &= \hat{\mathbf{N}} \cos I + \hat{\mathbf{z}}^{(m)} \cos\theta_z \, \sin I - \hat{\mathbf{u}}^{(m)} \sin\theta_z \, \sin I \end{aligned} \tag{A13}$$

The unit vector of the projection of $\hat{\mathbf{F}}$ upon the $\hat{u}^{(m)}$–$\hat{w}^{(m)}$–plane reads:

$$\hat{\mathbf{F}}_{p^{(m)}} = \cos\Delta^* \, \hat{\mathbf{u}}^{(m)} - \sin\Delta^* \, \hat{\mathbf{w}}^{(m)} \tag{A14}$$

Hence, $\hat{\mathbf{F}}$ takes the form:

$$\hat{\mathbf{F}} = a \, \hat{\mathbf{z}}^{(m)} + b \, (\hat{\mathbf{u}}^{(m)} \cos\Delta^* - \hat{\mathbf{w}}^{(m)} \sin\Delta^*) \tag{A15}$$

with yet unknown coefficients a and b. Obviously, a and b must always be real, and b must be non–negative, otherwise eq. (A15) would contradict eq. (A14). We obtain the relation between a and b from

$$1 = \hat{\mathbf{F}}^2 = a^2 + b^2(\cos^2\Delta^* + \sin^2\Delta^*) = a^2 + b^2$$
$$\Longrightarrow \quad a = \pm\sqrt{1-b^2} \tag{A16}$$

In order to simplify the following calculations we limit the module inclination, θ_z, to reasonable angles. We conducted our measurements in the northern hemisphere, in an area where $I \approx 60°$, and we require $\theta_z < I$. The latter guarantees $a \geq 0$, i.e. only the positive root is valid. In fact, in all our sea trials, θ_z was typically an order of magnitude smaller than I. Furtheron, the following relations hold

$$\begin{aligned} \hat{\mathbf{F}} \cdot \hat{\mathbf{u}}^{(m)} &= b\cos\Delta^* \\ \hat{\mathbf{F}} \cdot \hat{\mathbf{w}}^{(m)} &= -b\sin\Delta^* \\ \hat{\mathbf{F}} \cdot \hat{\mathbf{z}}^{(m)} &= a \end{aligned} \tag{A17}$$

From eq. (A13) we find

$$\begin{aligned} \hat{\mathbf{F}} \cdot \hat{\mathbf{u}}^{(m)} &= \hat{\mathbf{N}} \cdot \hat{\mathbf{u}}^{(m)} \cos I - \sin\theta_z \sin I \\ \hat{\mathbf{F}} \cdot \hat{\mathbf{w}}^{(m)} &= \hat{\mathbf{N}} \cdot \hat{\mathbf{w}}^{(m)} \cos I \\ \hat{\mathbf{F}} \cdot \hat{\mathbf{z}}^{(m)} &= \hat{\mathbf{N}} \cdot \hat{\mathbf{z}}^{(m)} \cos I + \cos\theta_z \sin I \end{aligned} \tag{A18}$$

On the right–hand side of eq. (A17), we express a through b using the result from eq. (A16). We then combine eq. (A17) with eq. (A18) in order to eliminate the vector products involving $\hat{\mathbf{F}}$. Consider now

$$1 = \hat{\mathbf{N}}^2 = (\hat{\mathbf{N}} \cdot \hat{\mathbf{u}}^{(m)})^2 + (\hat{\mathbf{N}} \cdot \hat{\mathbf{w}}^{(m)})^2 + (\hat{\mathbf{N}} \cdot \hat{\mathbf{z}}^{(m)})^2 \tag{A19}$$

We replace the three squared terms on the right–hand side of eq. (A19) with the corresponding terms obtained from eq. (A18). After a little algebra we arrive at the quadratic equation:

$$b^2 + 2Ab - C^2 = 0 \tag{A20}$$

in which we used the abbreviations

$$\begin{aligned} A &= \frac{\sin I \sin\theta_z \cos\Delta^*}{\sin^2\theta_z \cos^2\Delta^* + \cos^2\theta_z} \\ C^2 &= \frac{\cos^2\theta_z \; - \sin^2 I}{\sin^2\theta_z \cos^2\Delta^* + \cos^2\theta_z} \end{aligned} \tag{A21}$$

If we require $\theta_z + I < \pi/2$, a condition which was always fulfilled in our experiments, we find that C^2 is always positive. The general solution reads

$$b = -A \pm \sqrt{A^2 + C^2} \tag{A22}$$

Evaluation of the relation

$$A^2 + C^2 = \frac{\cos^2\theta_z(\cos^2\Delta^* \sin^2\theta_z + \cos^2\theta_z - \sin^2 I)}{(\sin^2\theta_z \cos^2\Delta^* + \cos^2\theta_z)^2} \geq 0 \tag{A23}$$

guarantees that b is real. As b must be non-negative, only the solution of eq. (A22) with the positively signed second term is valid. The magnetic variation unit vector, $\hat{\mathbf{B}}$, and the geomagnetic field unit vector, $\hat{\mathbf{F}}$, read in the $\hat{u}^{(m)}$–$\hat{w}^{(m)}$–$\hat{z}^{(m)}$–system

$$\begin{pmatrix} \hat{B}_{u^{(m)}} \\ \hat{B}_{w^{(m)}} \\ \hat{B}_{z^{(m)}} \end{pmatrix} = \begin{pmatrix} \cos\psi & \sin\psi & 0 \\ -\sin\psi & \cos\psi & 0 \\ 0 & 0 & 1 \end{pmatrix} \begin{pmatrix} \hat{B}_{x^{(m)}} \\ \hat{B}_{y^{(m)}} \\ \hat{B}_{z^{(m)}} \end{pmatrix} \tag{A24}$$

$$\begin{pmatrix} \hat{F}_{u^{(m)}} \\ \hat{F}_{w^{(m)}} \\ \hat{F}_{z^{(m)}} \end{pmatrix} = \begin{pmatrix} b\cos\Delta^* \\ -b\sin\Delta^* \\ \sqrt{1-b^2} \end{pmatrix} \tag{A25}$$

We rotate the $\hat{u}^{(m)}$–$\hat{w}^{(m)}$–$\hat{z}^{(m)}$–system by $-\theta_z$ around the $\hat{w}^{(m)}$–axis, in order to construct a new coordinate system, named the $\hat{u}^*$–$\hat{w}^{(m)}$–$\hat{z}^*$–system. Note that $\hat{\mathbf{z}}^* \equiv \hat{\mathbf{e}}_3$, i.e. the $\hat{u}^*$–$\hat{w}^{(m)}$–plane is the horizontal plane. The magnetic variation unit vector, $\hat{\mathbf{B}}$, reads in the $\hat{u}^*$–$\hat{w}^{(m)}$–$\hat{z}^*$–system:

$$\begin{pmatrix} \hat{B}_{u^*} \\ \hat{B}_{w^{(m)}} \\ \hat{B}_{z^*} \end{pmatrix} = \begin{pmatrix} \cos\theta_z & 0 & \sin\theta_z \\ 0 & 1 & 0 \\ -\sin\theta_z & 0 & \cos\theta_z \end{pmatrix} \begin{pmatrix} \hat{B}_{u^{(m)}} \\ \hat{B}_{w^{(m)}} \\ \hat{B}_{z^{(m)}} \end{pmatrix} \tag{A26}$$

The geomagnetic field unit vector, $\hat{\mathbf{F}}$, is formed the same way, using the same transformation matrix. With the help of eq. (A12), the projection of $\hat{\mathbf{F}}$ upon the $\hat{u}^*$–$\hat{w}^{(m)}$–plane, $\mathbf{F}_{p^*}$ (which is not a unit vector), can be expressed as

$$\mathbf{F}_{p^*} = \hat{\mathbf{N}} \cos I = (\hat{F}_{u^*}\hat{\mathbf{u}}^* + \hat{F}_{w^{(m)}}\hat{\mathbf{w}}^{(m)}) \cos I \tag{A27}$$

The angle φ between $\mathbf{F}_{p^*}$ and the $\hat{u}^*$–axis, signed positive when measured clockwise around the $\hat{z}^*$–axis from $\mathbf{F}_{p^*}$ to $\hat{\mathbf{u}}^*$, is determined by

$$\cos\varphi = \hat{\mathbf{N}} \cdot \hat{\mathbf{u}}^* = \frac{\hat{\mathbf{F}} \cdot \hat{\mathbf{u}}^*}{\cos I} = \frac{\hat{F}_{u^*}}{\cos I} = \frac{\cos\theta_z \hat{F}_{u^{(m)}} + \sin\theta_z \hat{F}_{z^{(m)}}}{\cos I}$$
$$= \frac{b\cos\theta_z \cos\Delta^* + \sqrt{1-b^2}\sin\theta_z}{\cos I}$$
$$-\sin\varphi = \hat{\mathbf{N}} \cdot \hat{\mathbf{w}}^{(m)} = \frac{\hat{\mathbf{F}} \cdot \hat{\mathbf{w}}^{(m)}}{\cos I} = \frac{\hat{F}_{w^{(m)}}}{\cos I} = \frac{-b\sin\Delta^*}{\cos I} \tag{A28}$$

Finally, we rotate the $\hat{u}^*$–$\hat{w}^{(m)}$–$\hat{z}^*$–system counterclockwise by φ (clockwise by $-\varphi$) around the $\hat{z}^*$–axis ($\equiv \hat{e}_3$–axis) and arrive at the $\hat{N}$–$\hat{E}$–$\hat{V}$–system. The following transform permits us to express the unit vector of the magnetic variation, $\hat{\mathbf{B}}$, in the latter system.

$$\begin{pmatrix} \hat{B}_N \\ \hat{B}_E \\ \hat{B}_V \end{pmatrix} = \begin{pmatrix} \cos\varphi & -\sin\varphi & 0 \\ \sin\varphi & \cos\varphi & 0 \\ 0 & 0 & 1 \end{pmatrix} \begin{pmatrix} \hat{B}_{u^*} \\ \hat{B}_{w^{(m)}} \\ \hat{B}_{z^*} \end{pmatrix} \tag{A29}$$

is the desired representation of $\hat{\mathbf{B}}$ in the geomagnetic north–east–vertical ($\hat{N}$–$\hat{E}$–$\hat{V}$)–system.

Occasionally, a further rotation of the coordinate system around the vertical axis is performed in order to align the two horizontal axes with directions imposed by the environment, e.g. the topography or geology. For measurement sites close to the coast, the coast–parallel and coast–perpendicular directions are an obvious choice. If the angle from magnetic north to the orientation of the coast line is denoted by γ (measured positive clockwise from north), a further matrix transformation needs to be applied to the magnetic field vector.

$$\begin{pmatrix} \hat{B}_{\parallel} \\ \hat{B}_{\perp} \\ \hat{B}_V \end{pmatrix} = \begin{pmatrix} \cos\gamma & \sin\gamma & 0 \\ -\sin\gamma & \cos\gamma & 0 \\ 0 & 0 & 1 \end{pmatrix} \begin{pmatrix} \hat{B}_N \\ \hat{B}_E \\ \hat{B}_V \end{pmatrix} \tag{A30}$$

is the desired representation of $\hat{\mathbf{B}}$ in a system where the three axes are oriented in the directions, coast–parallel, coast–perpendicular and vertical.

In summary, we have to proceed with the following sequence of computations in order to achieve our goal and arrive at a representation of the magnetic variation vector, **B**, in the geomagnetic north-east-vertical system

$$
\begin{aligned}
\cos\theta_z &= \sqrt{1-\sin^2\theta_x-\sin^2\theta_y} \\
\sin\theta_z &= \sqrt{\sin^2\theta_x+\sin^2\theta_y} \\
\cos\psi &= \sin\theta_x/\sin\theta_z \\
\sin\psi &= \sin\theta_y/\sin\theta_z \\
\sin\Delta^* &= \sin\Delta\cos\psi+\cos\Delta\sin\psi \\
\cos\Delta^* &= \cos\Delta\cos\psi-\sin\Delta\sin\psi \\
D &= \sin^2\theta_z\cos^2\Delta^*+\cos^2\theta_z \\
A &= (\sin I\sin\theta_z\cos\Delta^*)/D \\
C^2 &= (\cos^2\theta_z-\sin^2 I)/D \\
b &= -A+\sqrt{A^2+C^2} \\
\cos\varphi &= (b\cos\theta_z\cos\Delta^*+\sqrt{1-b^2}\sin\theta_z)/\cos I \\
\sin\varphi &= b\sin\Delta^*/\cos I
\end{aligned}
$$

After these computation steps have been completed (only once for every magnetometer and every site, i.e. for a fixed set of angles, θ_x, θ_x, Δ) we have to transform each **B**–vector in the time domain for each time datum according to the scheme

$$
\begin{pmatrix} B_{\parallel}(t) \\ B_{\perp}(t) \\ B_V(t) \end{pmatrix} = \begin{pmatrix} \cos\gamma & \sin\gamma & 0 \\ -\sin\gamma & \cos\gamma & 0 \\ 0 & 0 & 1 \end{pmatrix} \cdot \begin{pmatrix} \cos\varphi & -\sin\varphi & 0 \\ \sin\varphi & \cos\varphi & 0 \\ 0 & 0 & 1 \end{pmatrix}
$$

$$
\cdot \begin{pmatrix} \cos\theta_z & 0 & \sin\theta_z \\ 0 & 1 & 0 \\ -\sin\theta_z & 0 & \cos\theta_z \end{pmatrix} \cdot \begin{pmatrix} \cos\psi & \sin\psi & 0 \\ -\sin\psi & \cos\psi & 0 \\ 0 & 0 & 1 \end{pmatrix} \cdot \begin{pmatrix} B_{x(m)}(t) \\ B_{y(m)}(t) \\ B_{z(m)}(t) \end{pmatrix}
$$

Annex B

Estimating the coefficients of a linear trivariate model

We assume that a discrete time series, $u(t)$, can be expressed through a linear combination of three independent discrete time series, $x(t)$, $y(t)$ and $z(t)$, plus an uncorrelated term, $\delta u(t)$:

$$u(t) = \alpha x(t) + \beta y(t) + \gamma z(t) + \delta u(t) \tag{B1}$$

The residual sum of squares reads

$$\begin{aligned} Q^2 = \sum(\delta u)^2 &= \sum u^2 + \alpha^2 \sum x^2 + \beta^2 \sum y^2 + \gamma^2 \sum z^2 \\ &\quad - 2\left(\alpha \sum ux + \beta \sum uy + \gamma \sum uz\right) \\ &\quad + 2\left(\alpha\beta \sum xy + \beta\gamma \sum yz + \gamma\alpha \sum zx\right) \end{aligned} \tag{B2}$$

Taking partial derivatives yields the system

$$\begin{aligned} \frac{\partial Q^2}{\partial \alpha} &= 2\left[\alpha \sum x^2 - \sum ux + \beta \sum xy + \gamma \sum zx\right] \\ \frac{\partial Q^2}{\partial \beta} &= 2\left[\beta \sum y^2 - \sum uy + \alpha \sum xy + \gamma \sum yz\right] \\ \frac{\partial Q^2}{\partial \gamma} &= 2\left[\gamma \sum z^2 - \sum uz + \alpha \sum zx + \beta \sum yz\right] \end{aligned} \tag{B3}$$

In order to find that parameter set, α, β, γ, which minimizes Q^2, we solve the system of three normal equations

$$\begin{aligned} \frac{\partial Q^2}{\partial \alpha} &= 0 \\ \frac{\partial Q^2}{\partial \beta} &= 0 \\ \frac{\partial Q^2}{\partial \gamma} &= 0 \end{aligned} \tag{B4}$$

which can be rewritten as a system of three linear inhomogeneous equations with the three unknown variables, α, β, γ:

$$\begin{aligned} \alpha \sum x^2 + \beta \sum xy + \gamma \sum zx &= \sum ux \\ \alpha \sum xy + \beta \sum y^2 + \gamma \sum yz &= \sum uy \\ \alpha \sum zx + \beta \sum yz + \gamma \sum z^2 &= \sum uz \end{aligned} \tag{B5}$$

The system is solved using standard techniques of numerical mathematics.

The same procedure is applied to each of the three components of the magnetic field variation vector, where $u(t)$ stands for any of the test magnetometer vector components, and $x(t)$, $y(t)$ and $z(t)$ for the vector components of the reference magnetometer.

Annex C

Inverting test and reference sensor: The effect on the residual sum of squares

Let us assume that two different sensors, with identification numbers "1" and "2", record simultaneously N samples each of two discrete scalar time series, $v_1(t)$ and $v_2(t)$, consisting of different multiples of a common, time-varying stochastic signal, $s(t)$, and Gaussian white noise, $n_1(t)$ and $n_2(t)$, respectively:

$$\begin{aligned} v_1(t) &= c_1\, s(t) + n_1(t) \\ v_2(t) &= c_2\, s(t) + n_2(t) \end{aligned} \tag{C1}$$

Here, c_1 and c_2 are real constants (scale factors). The noise may stem from the system and from external noise sources which are uncorrelated with the signal and uncorrelated between both sensors. Signal and noise shall have the expectation values ($i, j \in \{1, 2\}$):

$$\begin{aligned} E\{s\} &= 0 \\ E\{s^2\} &= {\sigma_s}^2 \\ E\{n_i\} &= 0 \\ E\{{n_i}^2\} &= {\sigma_n}^2 \\ E\{s n_i\} &= 0 \\ E\{n_i n_j\} &= 0 \quad \text{for } i \neq j \end{aligned} \tag{C2}$$

The conditions listed in (C2) state that the noise variance is assumed to be identical at both sites. Each of the time series shall be expressed through the other in a linear univariate representation ($i, j \in \{1, 2\}$ and $i \neq j$):

$$v_j(t) = \alpha_i\, v_i(t) + \delta_j(t) \tag{C3}$$

where δ_j represents that part of v_j which is not linearly correlated with v_i. The residual sum of squares, ${Q_j}^2$, reads

$$Q_j{}^2 = \sum \delta_j{}^2 = \sum (v_j - \alpha_i v_i)^2 \tag{C4}$$

In order to find the minimum value of $Q_j 2$ (and thus the optimal regression coefficient, α_i) we take its derivative with respect to α_i

$$\frac{\partial Q_j{}^2}{\partial \alpha_i} = 2 \left[\alpha_i \sum v_i{}^2 - \sum v_i v_j \right] \tag{C5}$$

and solve the corresponding normal equation

$$\frac{\partial Q_j{}^2}{\partial \alpha_i} = 0 \quad \Longrightarrow \quad \alpha_i = \frac{\sum v_i v_j}{\sum v_i{}^2} \tag{C6}$$

We insert α_i into eq. (C4) and obtain

$$Q_j{}^2 = \frac{\sum v_i{}^2 \sum v_j{}^2 - (\sum v_i v_j)^2}{\sum v_i{}^2} \tag{C7}$$

Expansion of the terms on the right hand side yields

$$\begin{aligned} \sum v_i v_j &= c_i c_j \sum s^2 + c_i \sum s n_j + c_j \sum s n_i + \sum n_i n_j \\ \sum v_i{}^2 &= c_i{}^2 \sum s^2 + 2 c_i \sum s n_i + \sum n_i{}^2 \\ \sum v_j{}^2 &= c_j{}^2 \sum s^2 + 2 c_j \sum s n_j + \sum n_j{}^2 \end{aligned} \tag{C8}$$

Taking into consideration the conditions stated in eq. (C2), we find the asymptotic limits (i.e. the limits for $N \to \infty$) of the normalized versions of the three terms on the left-hand side of eq. (C8)

$$\begin{aligned} \lim_{N\to\infty} \left(\frac{1}{N} \sum v_i v_j \right) &= c_i c_j \sigma_s{}^2 \\ \lim_{N\to\infty} \left(\frac{1}{N} \sum v_i{}^2 \right) &= c_i{}^2 \sigma_s{}^2 + \sigma_n{}^2 \\ \lim_{N\to\infty} \left(\frac{1}{N} \sum v_j{}^2 \right) &= c_j{}^2 \sigma_s{}^2 + \sigma_n{}^2 \end{aligned} \tag{C9}$$

so that the expectation value of the univariate regression coefficient, α_i, reads

$$E\{\alpha_i\} = \frac{c_i c_j {\sigma_s}^2}{{c_i}^2 {\sigma_s}^2 + {\sigma_n}^2} \tag{C10}$$

Rewriting eq. (C7) with the normalized terms from eq. (C9) yields an asymptotic limit for the residual sum of squares

$$\lim_{N\to\infty} \left({Q_j}^2\right) = \frac{({c_i}^2 {\sigma_s}^2 + {\sigma_n}^2)({c_j}^2 {\sigma_s}^2 + {\sigma_n}^2) - {c_i}^2 {c_j}^2 {\sigma_s}^4}{{c_i}^2 {\sigma_s}^2 + {\sigma_n}^2} \tag{C11}$$

We apply the same procedure to ${Q_i}^2$ and find the asymptotic limit of the ratio between ${Q_j}^2$ and ${Q_i}^2$

$$\lim_{N\to\infty} \left(\frac{{Q_j}^2}{{Q_i}^2}\right) = \frac{{c_j}^2 {\sigma_s}^2 + {\sigma_n}^2}{{c_i}^2 {\sigma_s}^2 + {\sigma_n}^2} \tag{C12}$$

eq. (C12) lends support to the following interpretation: If, for instance, the time series v_2 has a larger variance than v_1, which is equivalent to requiring that the absolute value of c_2 exceeds that of c_1 (see eq. C9)), the ratio of the residual sums of squares, ${Q_2}^2/{Q_1}^2$, is asymptotically greater than 1, in other words, ${Q_2}^2$ exceeds ${Q_1}^2$. That means, expressing v_2 linearly through v_1 in a univariate way, c.f. eq. (C3), results in an asymptotically larger error than expressing v_1 linearly through v_2.

Annex D

Magnetometer system noise and its effect on the residuals

The distribution of the magnetic field residuals between neighbouring magnetometers operated in a magnetically quiet area provides us with an upper limit of the system noise over the bandwidth considered in this report, 1.5–80 mHz. Based on the results displayed in Fig. 10a, we assume a maximum of 0.25 nT for the system noise, ε_{T-R}, between two properly functioning magnetometers denoted by the subscripts T and R.

If all magnetometers are practically identical as far as the sensor system noise variance is concerned, the single sensor self noise is found according to:

$$\varepsilon_{T-R}^2 = \varepsilon_T^2 + \varepsilon_R^2 \quad \Longrightarrow \quad \varepsilon_T = \varepsilon_R = \frac{\varepsilon_{T-R}}{\sqrt{2}} = \frac{0.25}{\sqrt{2}} = 0.18\,\mathrm{nT} \qquad \text{(D1)}$$

We conclude that the system noise of each sensor component of each magnetometer is less than 0.2 nT in the bandwidth of interest.

Let us now consider a magnetic field residual, A_{obs}, computed from observations from the same vector component of two magnetometers, subscripted T and R, which are separated by a distance, D. The occurrence frequency of those residuals which exceed a certain threshold decreases rapidly with increasing threshold. We thus argue that the vast majority of observed excesses of an arbitrary threshold occurs when large system noise and true magnetic field residual add up.

$$A_{obs} = A_{true} + \varepsilon_{T-R} \quad \Longrightarrow \quad \frac{A_{true}}{D} = \frac{A_{obs} - \varepsilon_{T-R}}{D} \qquad \text{(D2)}$$

If we want to know what magnetic field residual would have been observed if the magnetometer spacing were normalized to a unit distance and the true residual had a constant spatial gradient (i.e. the residual were proportional to the distance), we need to find the true normalized amplitude, supplemented by a contribution from the sensor system noise which is independent of the sensor spacing. In doing so we arrive at the following:

$$\frac{A_{true}}{D} + \varepsilon_{T-R} = \frac{A_{obs}}{D} + \varepsilon_{T-R}\left(1 - \frac{1}{D}\right) \tag{D3}$$

According to this formula, the observed magnetic field residual, A_{obs}, would have to exceed a threshold, L_{obs}, given by

$$L_{obs} = D\,L_{unit} - \varepsilon_{T-R}(D-1) \tag{D4}$$

in order to find a unit-length spaced, but noise contaminated, residual (i.e. the left-hand side of eq. (D3)), to exceed a threshold, L_{unit}. The numbers for L_{obs} given in Table 5 of our report were computed for a threshold, $L_{unit} = 0.4$ nT, using eq. (D4).

Map 1 *The southern Ligurian coastal zone with magnetometer sites marked by black dots. The red dot in the inlay map of Italy indicates the geographic location of the measurement area. Bathymetry in metres.*

Map 2 *Montecristo island (Tyrrhenian Sea) and its easterly water space, with magnetometer sites marked by black dots. The red dot in the inlay map of Italy indicates the geographic location of the measurement area. Bathymetry in metres.*

Map 3 *The Formiche di Grosseto area (Tyrrhenian Sea) with part of Tuscany visible in the upper right corner. Magnetometer sites are marked by black dots. The red dot in the inlay map of Italy indicates the geographic location of the measurement area. Bathymetry in metres.*

Figure 1 *The magnetic dipole field of a submarine sailing at constant speed along a straight line, as it is seen by a vector magnetometer at a fixed location, is always and in all its vector components, composed of linear combinations of three simple algebraic functions named "Anderson functions". The coefficients of the linear compositions depend on the dipole strength and orientation, and the ship's velocity, heading, and distance from the magnetometer at the point of closest approach.*

Figure 2 *Magnetic field vector residuals for three pairs of OBMs, 04 19, 03 19 and 04 03 (see Map 2 for their locations). The residuals are basically the spatially uncorrelated components of magnetic field variations observed simultaneously at spaced sites. The relatively large excursion at 14:38 UTC marks the passage of the workboat* MANNING *across OBM 04. See the text for further explanations.*

Figure 3 *Mean peak-to-peak amplitudes of natural geomagnetic pc-type variations observed over many years at the Geophysical Institute Göttingen (F.R.G.). Such variations contribute to the always present geomagnetic noise and set a limit to the submarine detection capability if no ambient noise suppression is applied.*

Figure 4a *Temporal variation of the three vector components of the ambient magnetic field on a magnetically moderately disturbed day (upper panel) and a magnetically quiet day (lower panel), recorded with OBM 04 (marked "M04" in Map 3). The highlighted wavelets resemble in shape, amplitude and duration the magnetic field distortion generated by a passing ship (c.f. Figure 1).*

Figure 4b *Variation of the eastward component of the ambient magnetic field recorded simultaneously with three OBMs at spaced sites. The time intervals are identical to those shown in Figure 4a. OBM 18 and OBM 19 were located 2 km eastward and 6 km westward, respectively, of OBM 04 (see also Map 3). The magnetic field difference between OBM 04 and the mean of OBM 18 and 19 (bottom curve in each of the two panels) reveals that the noted wavelets were uniform over several kilometres distance (upper panel) and localized near OBM 04 (lower panel),*

respectively. The characteristics of the mean difference suggest that the wavelets were of ionospheric origin in the first case (upper panel), and generated by a passing ship in the second case (lower panel), respectively. The northward and vertical components of the magnetic variation were in principle similar to the eastward component and are not shown here.

Figure 5 *Diurnal distribution of the geomagnetic field variance near Deiva Marina, averaged over consecutive 15-min intervals. Only relative amplitudes are displayed. The measurements were made continuously over 16 days with a land-based magnetometer operated by A. Magunia (Universität Frankfurt/Main, F.R.G.) at about 500 m distance from the railway line. The small arrowheads along the top and bottom margins mark the separations we chose in order to break the day into four intervals with different levels of magnetic field variance (c.f. Table 4).*

Figure 6 *Magnetic field variations (coast–perpendicular component only) recorded simultaneously by the OBMs 17, 18, 19 and 12 which were aligned along a profile perpendicular to the coast and to a major railway line (which closely follows the coast line), see Map 1. The entire time interval (1600-1900 UTC, equivalent to 17:00-20:00 local time) is strongly affected by train noise which significantly exceeds the ambient magnetic noise form natural sources even at 8 km distance from the railway line. Leakage of the electric train return currents into the sea is the most likely source of the magnetic noise.*

Figure 7 *Schematic of the binning method used to create the distributions presented in Figures 8, 10 and 11. Each time the magnetic field variation, difference, or residual crosses a bin threshold in a direction away from the zero line, the counter is incremented.*

Figure 8 *Occurrence frequency distributions of the magnetic field variations, differences and residuals between two neighbouring tri-axial magnetometers. Each pair of neighbouring OBMs occupies one printed page. The OBM identification numbers appear on the right hand side. The logarithmic scale at the bottom relates colour to number of bin threshold crossings per hour ("events/hour"), c.f. Figure 7. The bin thresholds increase along the ordinate, the days (each having four diurnal intervals, c.f. Table 4) along the abscissa. Each residual panel is split into two subpanels, the upper one containing all data, the lower one the data cleaned for identified ship signatures, acoustic interrogation noise, and certain types of sensor noise (see also Tables 7 and 8). Figures 8a,b refer to the 1997 data from the magnetically quiet Montecristo area, Figures 8c-h to the 1996 data from the highly disturbed southern Ligurian coastal zone.*

Figure 9 *Variation of the ambient magnetic field (coast–parallel component), measured simultaneously with four OBMs located along a line perpendicular to the coast (modules 17, 18, 19 and 12, see Map 1). The highlighted section marks the passage*

of a single train on the coastal railway line. Yellow covers the interval when the train was on the rails between the power substations of Levanto and Sestri Levante, green the passing of the train through the railway station of Deiva Marina (without making a stop).

Figure 10 *Cumulative occurrence frequency distributions of magnetic field variations, differences and residuals between two neighbouring sites (1997 data, Montecristo area). Each panel displays the results from a specific vector component and a specific diurnal interval, averaged over the length of the entire sea trial. The term "events/hour" has the same meaning as in Figure 8: The bar diagram indicates how often a certain bin theshold, the size of which increases along the abscissa, is exceeded. The comparison between OBMs 17 and 19 is split into two parts, (I) and (II), in accordance with Figure 8a. 10a contains the data from the first part of the sea trial, up to July 23, and 10b the much noisier data from the second part, starting July 23. 10c, the comparison between OBMs 04 and 19, covers the entire length of the sea trial.*

Figure 11 *Like Figure 10 but for the 1996 data (southern Ligurian coast). For this figure, the bin sizes were normalized to a hypothetical sensor spacing of 1 km, taking into account the non-normalizable dual-sensor system noise (see Annex D for a detailed discussion). Therefore the abscissa does not start with 0 nT/km but with a certain offset which varies with the distance between the sensors in each pair.*

Figure 12 *Mean lifetime of magnetic field residuals between two neighbouring OBMs before they exceed 0.4 nT/km. The relevant OBM numbers are printed along the bottom of the figure. The threshold of 0.4 nT/km includes a distance-independent contribution of 0.25 nT, which is our estimate for the dual-sensor system noise. The bar diagram suggests short intervals of uninterrupted low residual amplitudes for the vertical magnetic field component and long intervals for residuals between the coast-perpendicular component from two magnetometers having the same distance from coast.*

Document Data Sheet

NATO UNCLASSIFIED

Security Classification		Project No.
UNCLASSIFIED		061-1
Document Serial No.	**Date of Issue**	**Total Pages**
SR-304	February 1999	80 pp.

Author(s)

Watermann, J., Lam, J.

Title

Distributions of magnetic field variations, differences and residuals.

Abstract

Temporal and spatial variations of the geomagnetic field were recorded in different geographic areas, using arrays of seven tri-axial magnetometers which resided on the sea bottom in 50-150 m depth for periods up to 16 days. The different geographic areas are characterized by different levels of the mean ambient magnetic noise. We discuss briefly data from a magnetically quiet area and then focus on a coastal zone highly disturbed by anthropogenic magnetic fields, in particular by noise from a busy coastal electrified railway line. In the latter area, the spatial uniformity of the ambient magnetic field is rather poor and the correlation between adjacent sites lower than in the former one.

Simultaneous magnetic field observations from pairs of neighbouring magnetometers are analysed and compared in detail. We compute first vector differences of the magnetic variations measured at neighbouring sites, and subsequently vector residuals. The residuals are those contributions to the magnetic field variations which are not correlated between adjacent sites and which can not be represented through a linear trivariate model.

In the magnetically quiet area, we find that the magnetic field residuals are of the order of the system noise for magnetometers with about 1 km spacing and slightly higher for those with 12 km spacing. The area lends support to the application of a Remote Reference Technique, i.e. a technique in which the ambient magnetic field is compensated for by using measurements from a remotely operated reference sensor. "Remote" means that the reference sensor is sufficiently far away so that it is not influenced by the magnetic field of a ship navigating in the vicinity of the surveillance magnetometers.

Although the magnetic field variations in the highly disturbed coastal zone are several times larger than typical magnetic field variations of natural origin, and also spatially non-uniform, we find good linear correlation between adjacent sites. This is demonstrated by the often rather small magnetic field residuals. However, in order to achieve small residuals, the spacing between the magnetometers must be an order of magnitude smaller than in the quiet zone. This may require the use of a Local Reference Technique for compensation of the ambient magnetic field. In a Local Reference Technique, the reference sensor must be so close to the surveillance sensors that it, too, is influenced by the magnetic field of the submarine navigating in the vicinity of the surveillance sensors.

In the coastal zone, we find that the residuals of the vertical component of the magnetic field variations remain rather large. The coast-perpendicular component of magnetometers at equal distance from the coast yields the smallest residuals, i.e. they yield the best compensation of magnetic field variations when using a reference technique. The intensity distribution of magnetic field variations observed at the various sites strongly suggests that a significant part of the electric leakage currents from the railway system flows out into the sea, up to several kilometres off the shore.

In summary, we find that magnetic field variations in the southern Ligurian coastal zone are dominated by magnetic railway noise which results in an anisotropic distribution of the spatial correlation between spaced sites.

Issuing Organization

North Atlantic Treaty Organization
SACLANT Undersea Research Centre
Viale San Bartolomeo 400, 19138 La Spezia, Italy

[From N. America: SACLANTCEN (New York) APO AE 09613]

Tel: +39 0187 527 361
Fax:+39 0187 524 600

E-mail: library@saclantc.nato.int

Initial Distribution for SR-304

Ministries of Defence

DND Canada	10
CHOD Denmark	8
MOD Germany	15
HNDGS Greece	12
MARISTAT Italy	9
MOD (Navy) Netherlands	12
NDRE Norway	10
MOD Portugal	5
MDN Spain	2
TDKK and DNHO Turkey	5
MOD UK	20
ONR USA	32

NATO Commands and Agencies

NAMILCOM	2
SACLANT	3
CINCEASTLANT/ COMNAVNORTHWEST	1
CINCIBERLANT	1
CINCWESTLANT	1
COMASWSTRIKFOR	1
COMSTRIKFLTANT	1
COMSUBACLANT	1
SACLANTREPEUR	1
SACEUR	2
CINCNORTHWEST	1
CINCSOUTH	1
COMEDCENT	1
COMMARAIRMED	1
COMNAVSOUTH	1
COMSTRIKFORSOUTH	1
COMSUBMED	1
NC3A	1
PAT	1

Scientific Committee of National Representatives

SCNR Belgium	1
SCNR Canada	1
SCNR Denmark	1
SCNR Germany	1
SCNR Greece	1
SCNR Italy	1
SCNR Netherlands	2
SCNR Norway	1
SCNR Portugal	1
SCNR Spain	1
SCNR Turkey	1
SCNR UK	1
SCNR USA	2
SECGEN Rep. SCNR	1
NAMILCOM Rep. SCNR	1

National Liaison Officers

NLO Canada	1
NLO Denmark	1
NLO Germany	1
NLO Italy	1
NLO Netherlands	1
NLO Spain	1
NLO UK	1
NLO USA	1

Sub-total	188
SACLANTCEN	30
Total	218